

CREATE: Cross-Layer Resilience Characterization and Optimization for Efficient yet Reliable Embodied AI Systems

Tong Xie

School of Integrated Circuits
Peking University
Beijing, China
xietong@stu.pku.edu.cn

Zishen Wan

Georgia Institute of Technology
Atlanta, GA, USA
zishenwan@gatech.edu

Shaofei Cai

Institute for Artificial Intelligence
Peking University
Beijing, China
caishaofei@stu.pku.edu.cn

Yuan Wang

School of Integrated Circuits
Peking University
Beijing, China
wangyuan@pku.edu.cn

Yijiahao Qi

School of EECS
Peking University
Beijing, China
qiyijiahao@stu.pku.edu.cn

Yanchi Dong

School of Integrated Circuits
Peking University
Beijing, China
dongyangchi@pku.edu.cn

Yitao Liang

Institute for Artificial Intelligence
Peking University
Beijing, China
yitaol@pku.edu.cn

Runsheng Wang

School of Integrated Circuits
Peking University
Beijing, China
r.wang@pku.edu.cn

Jinqi Wen

School of EECS
Peking University
Beijing, China
2200012451@stu.pku.edu.cn

Zihao Wang

Institute for Artificial Intelligence
Peking University
Beijing, China
zhwang@stu.pku.edu.cn

Tianyu Jia

School of Integrated Circuits
Peking University
Beijing, China
tianyuj@pku.edu.cn

Meng Li*

Institute for Artificial Intelligence
Peking University
Beijing, China
meng.li@pku.edu.cn

Abstract

Embodied Artificial Intelligence (AI) has recently attracted significant attention as it bridges AI with the physical world. Modern embodied AI systems often combine a Large Language Model (LLM)-based planner for high-level task planning and a reinforcement learning (RL)-based controller for low-level action generation, enabling embodied agents to tackle complex tasks in real-world environments. However, deploying embodied agents remains challenging due to their high computation requirements, especially for battery-powered local devices. Although techniques like lowering operating voltage can improve energy efficiency, they can introduce bit errors and result in task failures.

*Corresponding author



This work is licensed under a Creative Commons Attribution 4.0 International License.

ASPLOS '26, March 22–26, 2026, Pittsburgh, PA, USA

© 2026 Copyright held by the owner/author(s).

ACM ISBN 979-8-4007-2359-9/2026/03

<https://doi.org/10.1145/3779212.3790147>

In this work, we propose CREATE, a general design principle that leverages heterogeneous resilience at different layers for synergistic energy-reliability co-optimization. For the first time, we conduct a comprehensive error injection study on modern embodied AI systems and observe an inherent but heterogeneous fault tolerance. Building upon these insights, we develop an *anomaly detection and clearance* mechanism at the circuit level to eliminate outlier errors. At the model level, we propose a *weight-rotation-enhanced planning* algorithm to improve the fault tolerance of the LLM-based planner. Furthermore, we introduce an application-level technique, *autonomy-adaptive voltage scaling*, to dynamically adjust the operating voltage of the controllers. The voltage scaling circuit is co-designed to enable online voltage adjustment. Extensive experiments demonstrate that without compromising task quality, CREATE achieves 40.6% computational energy savings on average over nominal-voltage baselines and 35.0% over prior-art techniques. This further leads to 29.5% to 37.3% chip-level energy savings and approximately a 15% to 30% improvement in battery life.

CCS Concepts: • Hardware → Robustness; • Computer systems organization → Architectures; Embedded and cyber-physical systems.

Keywords: Embodied AI System; Efficiency; Reliability; Resilience Characterization; Cross-layer Optimization

ACM Reference Format:

Tong Xie, Yijiahao Qi, Jinqi Wen, Zishen Wan, Yanchi Dong, Zihao Wang, Shaofei Cai, Yitao Liang, Tianyu Jia, Yuan Wang, Runsheng Wang, and Meng Li. 2026. CREATE: Cross-Layer Resilience Characterization and Optimization for Efficient yet Reliable Embodied AI Systems. In *Proceedings of the 31st ACM International Conference on Architectural Support for Programming Languages and Operating Systems, Volume 2 (ASPLOS '26), March 22–26, 2026, Pittsburgh, PA, USA*. ACM, New York, NY, USA, 18 pages. <https://doi.org/10.1145/3779212.3790147>

1 Introduction

Embodied artificial intelligence (AI) is a class of intelligent systems capable of understanding, reasoning, and interacting with the physical world [1–3]. Distinguished by their proficiency in executing complex long-horizon, multi-objective tasks, these systems have demonstrated broad application potential across various domains, including industrial manufacturing [4], logistics and transportation [5], and search-and-rescue operations [6]. As shown in Fig. 1(a), to achieve such capabilities, embodied agents typically employ large language models (LLMs) or multi-modal language models (MLMs) as *planners* to decompose the entire *tasks* into specific *subtasks*, alongside reinforcement learning (RL)-based *controllers* to determine low-level actions for each subtask, which typically requires thousands of *steps* [4, 7–12]. Task performance is usually measured by the success rate and average completion steps [4, 9–13].

Unlike traditional robotic systems driven by predefined rules [14, 15], embodied agents leverage large-scale LLMs, which would often consume trillions of operations per inference. Although cloud-based inference via APIs enables access to giant LLMs, e.g., GPT-4 [16], it introduces high communication latency and reliance on Wi-Fi, limiting desirable real-time interaction capabilities for many applications. Therefore, recent research has begun to explore the end-to-end deployment of embodied agents on edge hardware, such as GPUs [8, 17, 18] and customized accelerators [4, 7, 13, 19, 20], such as TPU-like systolic arrays [21, 22].

However, such edge deployment of embodied AI systems is often strictly energy-constrained due to reliance on battery power [1, 19, 20, 23, 24]. With intensive computational workloads (e.g., long-context LLM inference and high-frame-rate image processing), these computation platforms have been extensively reported to consume substantial power [4, 8, 13, 14, 25–30]. For example, [30] reported that the computing platform accounted for over 50% of total power on quadruped robots [31], and [13] demonstrated that LLM inference dominated the total energy consumption in a representative robotic setup using an NVIDIA GPU and Franka robot arm [26, 27, 32]. Therefore, it is imperative to improve the power efficiency of embodied AI systems. Given the quadratic relation between power consumption and operating

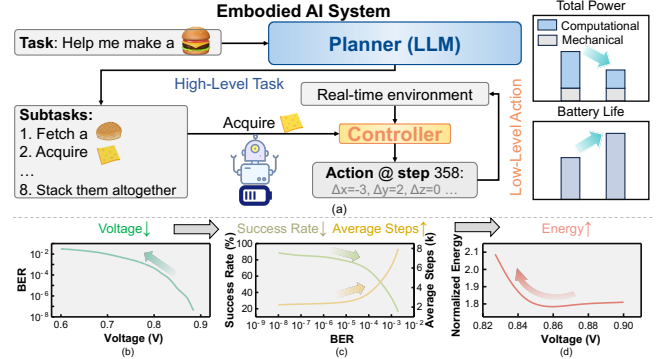


Figure 1. Embodied AI System Overview. (a) Embodied AI systems employ a hierarchical paradigm to tackle complex tasks: an LLM-based planner decomposes a task (often described in texts) into subtasks; then for each subtask, a low-level controller generates detailed actions step by step. These systems are typically battery-powered. (b) Lowering operating voltage introduces bit errors, causing (c) significant task performance degradation (e.g., lower task success rates and more task execution steps). (d) This in turn leads to higher energy consumption per task.

voltage, directly reducing the voltage can improve processing efficiency. This method, however, can induce timing violations [33–36] and increase computation bit error rates (BERs), as shown in Fig. 1(b), leading to severe degradation of task performance, such as lower task success rates and more execution steps (Fig. 1(c)). These can ultimately increase the energy consumption to complete a single task (Fig. 1(d)).

Various techniques have been proposed to balance reliability with efficiency at the circuit, algorithm, and system levels [37–56], but all remain prohibitively costly or impractical for embodied AI systems. Unlike traditional robotics, modern embodied agents are predominantly based on AI and deep neural networks (DNNs), which exhibit inherent error resilience [53, 57–62]. For example, as in Fig. 1(c), task success rates (stone in [11]) do not immediately degrade under low BERs, suggesting opportunities to save energy by strategically reducing the operating voltage without compromising the task performance. However, the error resilience of embodied AI systems is not well characterized yet, making it hard to determine a proper voltage scaling policy. While prior studies have examined the resilience of individual DNNs (e.g., convolutional neural networks (CNNs), RL algorithms, etc) [57–60] and traditional robotic systems [55, 56], the complex collaborations among diverse models as well as the sophisticated applications in embodied AI systems can produce fundamentally different resilience behaviors.

Therefore, to enable efficient yet reliable embodied AI systems through voltage scaling, for the first time, we perform large-scale error injection experiments to systematically characterize their error resilience. Our investigation reveals inherent but heterogeneous system robustness: while

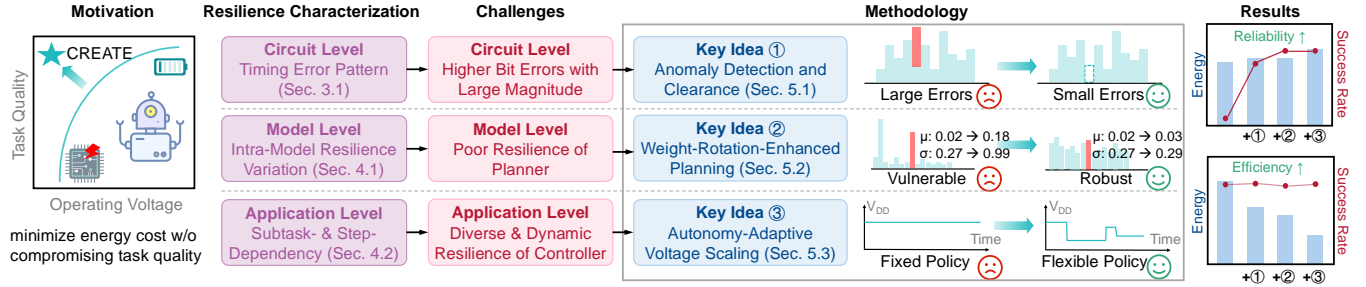


Figure 2. CREATE Overview. CREATE is a general design principle to enable efficient yet reliable embodied AI systems. At the circuit level, *anomaly detection and clearance* mitigate large timing errors. At the model level, *weight-rotation-enhanced planning* redistributes LLM activations to improve robustness. At the application level, *autonomy-adaptive voltage scaling* dynamically adjusts voltage based on task demands. These techniques collectively boost both reliability and efficiency.

both the planner and the controller show good error robustness at low BERs (e.g., $\leq 10^{-7}$), the controller exhibits much higher resilience at higher BERs. (e.g., 10^{-7} to 10^{-3}). We also analyze the resilience variation of different network components in the planner and controller, as well as dependency on subtasks and execution status. We observe that the systematic activation outliers in the LLM, when combined with the subsequent normalization operations, are the root cause of the planner’s poor resilience at higher BERs. Meanwhile, the controller exhibits varying resilience patterns across different subtasks and action steps during task execution.

Building on these insights, we propose CREATE, a general design principle that synergistically integrates optimizations across circuit, model, and application levels to work progressively, as illustrated in Fig. 2. At the **circuit level**, we introduce an *anomaly detection and clearance* mechanism to suppress large errors induced by timing violations, which serves as a solid foundation for subsequent optimizations although conceptually simple. However, smaller yet still critical errors, arising from the activation distributions of the LLM planner, persist and degrade performance. To address this, at the **model level**, we propose *weight-rotation-enhanced planning* to redistribute activation patterns of the LLM planner and improve robustness. To further optimize energy efficiency of the controller, at the **application level**, we propose *autonomy-adaptive voltage scaling*, which employs a flexible voltage control policy based on the current subtask execution status. We further customize a circuit for dynamic voltage scaling in systolic arrays and low-dropout regulators (LDOS) to holistically implement these optimizations. Our contributions can be summarized as follows:

- We conduct a comprehensive error injection study on representative embodied AI systems to analyze the impact of voltage-scaling-induced errors on task performance. Our analysis reveals that the controller demonstrates significantly better error resilience than the planner. We further investigate the resilience behaviors across different network components and execution steps. To the best of our knowledge, this is the

first comprehensive study of embodied AI system’s error resilience.

- We introduce CREATE, a general design principle that exploits the heterogeneous error resilience of embodied AI systems with cross-layer optimizations to minimize energy consumption without compromising their reliability and task performance. This framework is implemented via a customized circuit and LDOS.
- Extensive experiments demonstrate CREATE significantly improves error tolerance and energy efficiency while achieving generality across diverse tasks and voltage conditions. By aggressively lowering the operating voltage, CREATE achieves an average 40.6% improvement in computational energy efficiency over the nominal-voltage operation and 35.0% over state-of-the-art (SOTA) methods, translating to 29.5% to 37.3% chip-level energy savings and about 15% to 30% longer battery life, all with iso-task quality.

2 Background

2.1 Embodied Agents Overview

Embodied agents are a category of intelligent systems that rely on physical entities to understand, reason, and interact with the physical world [1–3]. Embodied agents take advantage of the generalization and reasoning capabilities of LLMs to handle complex tasks and typically comprise two core components: a planner and a controller [4, 7–12].

The **planner**, often a fine-tuned LLM or MLM, is responsible for comprehending tasks and decomposing them into a series of specific subtasks, known as high-level planning. These subtasks are then passed to the **controller**, typically a smaller RL model assigned to low-level control. The controller samples actions based on its output *action logits* in each step. This paradigm has been widely adopted in recent research [4, 7–9, 11, 12, 27], as listed in Table 1. In parallel, end-to-end vision-language-action (VLA) model is another prevalent approach, which directly generates action tokens or invokes APIs [10, 26, 27]. Additionally, many studies focus on models for low-level motion control [18, 64, 68, 75, 79].

Table 1. Representative Embodied Agent Systems that CREATE Can Support

Embodied System	Planner		Controller		Tasks		
	Model	#Params (B)	Model	Architecture	Description	Example	Benchmark
SayCan [7]	PaLM [63]	540	MT-Opt [64]	CNN	navigation	"move to the table"	ALFRED [65]
PaLM-E [8]	PaLM-E [8]	562	MT-Opt [64]	CNN	manipulation	"place water bottle upright"	Language-Table [66]
LLM-Planner [9]	GPT-3 [67]	175	HLSM [68]	Transformer	navigation	"move to the table"	ALFRED [65]
RT-2 [4]	PaLI-X [69]	55	RT-1 [18]	Transformer	manipulation	"place water bottle upright"	Language-Table [66]
Voyager [10]	GPT-4 [16]	1,760	-	-	multi-task	"obtain an iron sword"	Minecraft [70]
OpenVLA [26]	LLaMA [71]	7	-	-	mult-task	"put bottle on top of cabinet"	LIBERO [72]
RoboFlamingo [27]	OpenFlamingo [73]	3	-	-	mult-task	"pull handle to open drawer"	CALVIN [74]
Octo [75]	-	-	Octo [75]	Transformer	mult-task	"bring me 3 different sodas"	OXE [76]
LEO [77]	Vicuna [78]	7	ScanRefer [79]	Transformer	navigation	"find the toilet"	HM3D [80]
JARVIS-1 [11]	LLaVA [71]	8	STEVE-1 [81]	Transformer	mult-task	"obtain an iron sword"	Minecraft [70]

Despite these differences, VLAs and motion-control models are functionally analogous to the planner and controller, respectively, and thus align with the same overarching framework. The capabilities of such systems are typically evaluated through standardized simulation benchmarks, such as [65, 66, 70, 72, 74, 76, 80].

As listed in Table 1, modern embodied agents commonly employ LLM-based planners together with Transformer-based controllers for superior multi-task learning capacity [4, 18, 20, 24, 68, 81]. However, many such systems [4, 7–10] rely on massive (> 50 B parameters) planners running on cloud servers, making error-injection studies prohibitively expensive or inaccessible. Moreover, we argue that target tasks should be sufficiently complex and diverse, beyond simple grasping or navigation, to thoroughly assess agent performance. Therefore, in this paper, we select JARVIS-1 [11]—a representative open-world agent in Minecraft [70] that meets all these requirements—as our primary testbed for resilience characterization. We further evaluate our method across multiple embodied AI systems [18, 26, 27, 75] to validate the broad applicability.

Fig. 3 depicts the JARVIS-1 platform, where the LLM planner and controller, both of which consist of stacked Transformer layers with various *network components* (denoted as K, Down, etc.), work collaboratively within the Minecraft playground. The agent needs to interact with a dynamic 3D environment to acquire tasked items, typically requiring 5~20 basic subtasks, each involving hundreds of action steps. For instance, to obtain an enchanted golden apple, the planner would break it down into subtasks (e.g., mine logs, craft stone pickaxe, smelt golden ingots) to be executed by the controller in sequence. We refer interested readers to [11] for more detailed description of the JARVIS-1 platform and Minecraft tasks. Following [11], if a subtask remains incomplete after 600 steps, the planner will be re-invoked to adjust the subtask. The high-level task is deemed a failure upon exceeding 12,000 total steps.

In this paper, we evaluate the task quality on multiple Minecraft tasks [10, 11], ranging from fundamental objectives (e.g., wooden pickaxe, stone pickaxe, etc) to complex

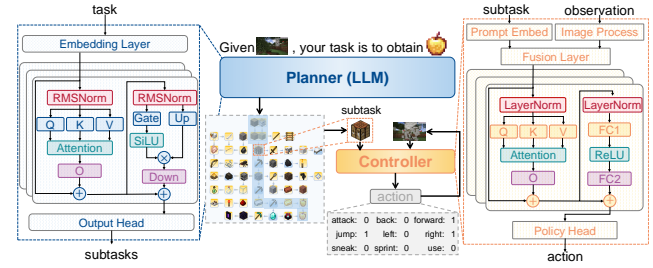


Figure 3. JARVIS-1 Platform. JARVIS-1 consistently acquires high-level items in Minecraft playground. The planner generates a subtask sequence, while the controller integrates subtask prompts with visual observations to determine actions at each step. Both the planner and controller are primarily stacked Transformer blocks, which contain various network components, such as K and Down.

ones (e.g., iron sword, cooked chicken, etc), each featuring distinct trajectories and biomes. These tasks are abbreviated as a single teletype word (e.g., wooden) throughout this paper. To mitigate execution randomness, each trial is repeated at least 100 times. Task quality is measured by success rate (\uparrow) and average steps (\downarrow), while system efficiency is assessed by average power and total energy consumption.

2.2 Computing Platforms of Embodied AI systems

In embodied AI systems, both the planner and controller are typically implemented with DNNs, whose core operations involve dense general matrix multiplications (GEMMs). To meet stringent energy requirements and real-time latency constraints, these DNNs are often deployed on local GPUs [8, 17, 18] or on specialized edge accelerators such as TPU-like systolic arrays [4, 7, 13, 20–22]. In many cases, GEMMs are quantized to low-precision (e.g., INT8) [82–88] to reduce power consumption, particularly in battery-powered systems that must continuously interact with dynamic environments. In our paper, we consider deploying the entire embodied AI system on a systolic array-based accelerator in INT8 format, a standardized and prevalent configuration [21, 40, 42, 58, 89, 90]. The planner and controller are orchestrated to execute in a coordinated pipeline.

2.3 Fault Tolerance Study

Error Sources. In embodied AI systems, both the memory and logic circuits are susceptible to reliability issues as CMOS technology scales to the nanoscale. Lowering the operating voltage exacerbates this problem: in on-chip SRAMs, reduced voltage noise margins lead to memory bit flips [53, 57, 58, 91], where in logic circuits, voltage underscaling prolongs path delays that would result in timing violations and incorrect outputs [35, 40, 47, 89]. Given that logic circuits typically dominate on-chip power consumption in compute-intensive workloads [22, 92, 93] and that the dynamic nature of embodied AI workloads creates meaningful opportunities for computational optimization, this work focuses on transient computational errors during inference induced by voltage underscaling. Extending timing-based resilience to memory components remains promising for future research.

Model Resilience Study. Generally speaking, error resilience refers to the ability of an algorithm to tolerate errors, typically quantified by the relationship between BER and model performance [58, 60]. Many studies [89, 90, 94–97] have adopted random bit-flip models as an abstraction to characterize the inherent resilience of DNNs and autonomous systems. For instance, [57] analyzed error propagation in DNNs while [58] explored the relationship between error impacts and data types. [59] identified heterogeneous vulnerabilities across network components and proposed selective protection. [53, 60] extended resilience analysis to RL-based applications and autonomous systems. [61, 62] characterized the resilience of individual LLMs and [56] assessed the risk of memory errors in robotic motion planning. However, due to the diversity and collaboration among models, and the complexity of executed tasks, the resilience behavior of an embodied agent system may exhibit distinct characteristics.

Error Mitigation Techniques. Error correction code (ECC) [98] can effectively address hardware faults in memory or on-chip buffers. Mitigating transient faults in computational datapaths is more challenging [47, 60, 96, 97], where various levels of protection can be applied. These methods, though effective in particular scenarios, incur prohibitive hardware or runtime overhead, especially in the context of embodied agents. For example, at the **circuit level**, redundancy-based approaches, e.g., dual modular redundancy (DMR) [37–39], are widely adopted in autonomous vehicles for error detection but require multiple copies of computations to be performed. Timing-borrowing methods [43–45] integrate shadow flip-flops (FFs) to detect timing errors in conventional circuits, yet lack scalability for large-scale accelerators. Although some approaches target accelerators, they either require prior knowledge of hardware specification [41, 42] or introduce significant hardware overheads [40], which hinders their applicability for online timing-error mitigation. At the **algorithm level**, fault-aware retraining, while effective for CNNs [50–52] and simple RL algorithms [53, 60], is

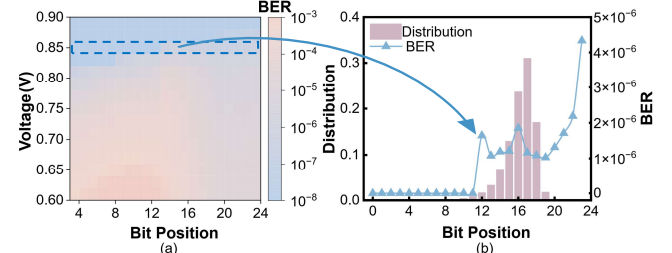


Figure 4. Timing error model. (a) Bit-level timing error rate under different voltages. (b) Error pattern at 0.85V, overlapping with normal runtime activation distribution.

impractical for embodied agents because of unacceptable retraining costs. Lightweight error detection and correction algorithms, such as algorithm-based fault tolerance (ABFT) and its variants [46–49], are suitable for GEMM operations but often require recomputation for error recovery, potentially violating real-time constraints. At the **system level**, application-specific protection strategies [54–56] for robotics or autonomous systems are tailored to rule-based dataflow and may hardly transfer seamlessly to DNN-driven embodied agents, which may exhibit distinct resilience characteristics.

3 Timing Error Modeling and Injection

3.1 Error Models

Since memory faults can be effectively mitigated by ECC [59, 60, 96, 97, 99], we focus on transient computational errors during inference, assuming data are correctly fetched from memory. To model timing errors, we adopt the widely used random bit-flip model [89, 94–96] as an abstraction, with error severity parameterized by BERs. To capture error patterns under different voltages, we synthesize an 8-bit multiplier/24-bit accumulator systolic array with commercial 22nm PDK (nominal voltage: 0.9V) and perform a detailed timing analysis using Synopsys PrimeTime and HSPICE. The error pattern is shown in Fig. 4(a), which aligns with prior chip measurements [43, 53, 62, 89]. As Fig. 4 illustrates, **higher bits exhibit frequent large timing errors** that cause severe performance degradation, whereas **lower bits errors exist within the ordinary runtime data range**. This correlates with the intuition that higher bits typically have longer carry chains and longer path delays [35, 89].

3.2 Error Injection Method

We implement a dynamic error-injection framework in PyTorch that emulates bit flips as runtime tensor operations, as commonly used in prior works [89, 94–97]. Following [82], inputs to GEMM and convolution layers in both the planner and controller are quantized to INT8, and errors are injected into their outputs. For resilience characterization (Sec. 4), we employ a uniform error model under varying BERs to isolate algorithmic resilience from hardware-specific dependencies and derive more generalizable conclusions. In Sec. 6, we build a look-up table based on Fig. 4(a) to more accurately capture voltage-induced timing errors.

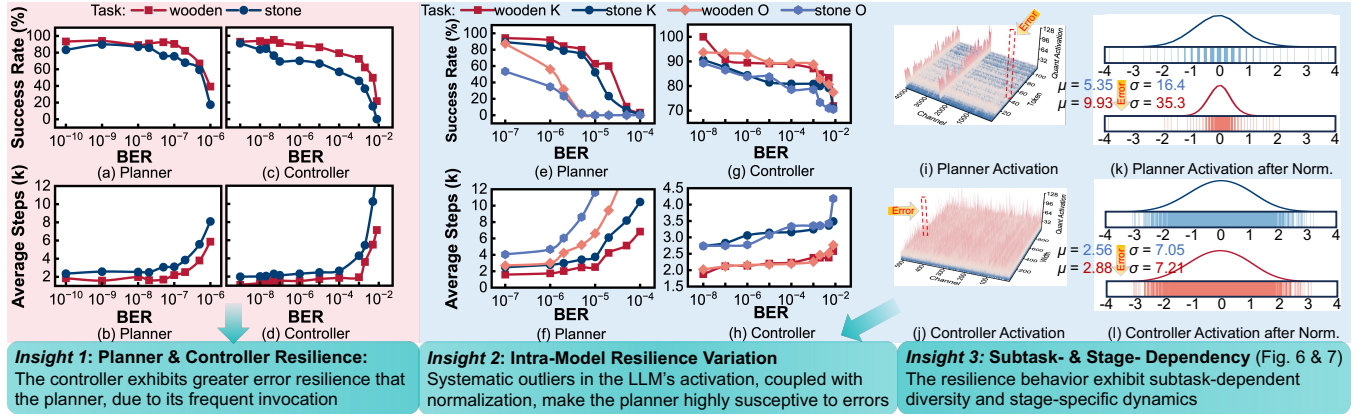


Figure 5. Resilience Characterization. (a)-(b) Planner resilience characteristics. (c)-(d) Controller resilience characteristics. (e)-(f) Resilience comparison between K and O in the planner. (g)-(h) Resilience comparison between K and O in the controller. (i)-(j) Activation distributions of the pre-norm layer in the planner and controller. (k) Planner normalization outcomes exhibit significant skew under errors; (l) Controller normalization maintains moderate variance.

4 Resilience Characterization

In this section, we present our resilience characterization on embodied AI systems, addressing the following questions:

Model-level Q1: What are the resilience characteristics of the planner and controller, and how do they differ?

Model-level Q2: Furthermore, how does resilience vary among different network components, within the planner and the controller?

Application-level Q3: How does resilience behavior dynamically change across subtasks and execution steps?

4.1 Model-level Resilience Characterization

Resilience Characteristic of Planner. We first inject errors into the planner to evaluate its resilience. Figs. 5(a) and (b) show that success rates plunge near $BER = 2 \times 10^{-8}$ for both tasks, while average steps rise significantly, indicating limited error tolerance. Two factors contribute: (i) the planner is invoked only once to guide multiple agent steps, so that a single misleading instruction can lead to prolonged irrelevant or incorrect actions; and (ii) as an LLM, the planner's output quality encounters severe deterioration under higher BER, producing irrelevant or nonsense text that hinders the controller. Further analysis will be provided later.

Resilience Characteristic of Controller. Similarly, we assess the controller's resilience by tracking the success rate and average steps under varying BER in Figs. 5(c)-(d). A notable drop in success rate and a corresponding rise in average steps emerge around $BER = 1 \times 10^{-4}$, underscoring the controller's critical impact on task performance yet also revealing notable error tolerance. This behavior can be explained from two perspectives as well: (i) the frequent invocation of the controller confines error effects within individual steps and allows correction in subsequent decisions; (ii) the controller can tolerate suboptimal decisions, as multiple feasible actions may be valid per step.

Discussion. By comparing Figs. 5 (a)-(b) with (c)-(d), we conclude that the controller exhibits significantly greater error resilience than the planner, owing to its more frequent invocation.

Resilience of different network components. This section explores the internal resilience of the planner and controller by injecting errors into individual network components (e.g., Q and FC1) within a Transformer layer. In the LLM planner, the components followed by normalization (including O and Down) exhibit noticeably poorer resilience than their counterparts without normalization (e.g., K), as shown in Figs. 5(e)-(f). In contrast, the controller displays only minor variations across components (Figs. 5(g)-(h)).

This disparity arises from distinct activation distributions. LLMs beyond billions of parameters are extensively reported to produce systematic outliers with much larger magnitudes [82, 85, 86] (Fig. 5(i)), whereas the controller's activations remain more uniform (Fig. 5(j)). Therefore, in the planner, normalization parameters, i.e., μ and σ , are subject to these outliers, whereas in the controller, they are more evenly determined across elements. When a single hardware fault occurs and introduces a larger error in LLM computations, these parameters may be drastically skewed (e.g., μ from 5.36 to 9.93 in Fig. 5 (k)), significantly distorting normalization outcomes. In contrast, the skew in the controller is relatively more moderate (e.g., σ from 7.05 to 7.21 in Fig. 5(l)), limiting its impact on the outcome.

Discussion. We conclude that outliers in the LLM's activation, coupled with subsequent normalization, make the planner highly susceptible to errors.

4.2 Application-level Resilience Characterization

Embodied agents typically accomplish high-level goals through consecutive sequences of subtasks—often hundreds of steps long. This subsection examines the controller's resilience across diverse subtasks and execution steps.

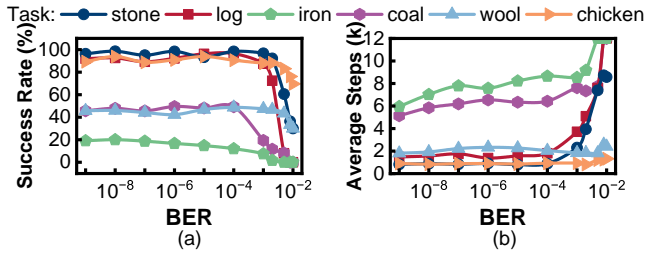


Figure 6. Different subtasks exhibit diverse resilience.

Resilience Diversity across Subtasks. We evaluate resilience across subtasks by injecting errors into controllers performing distinct subtasks in Fig. 6. Results reveal divergent behaviors: subtasks `log` and `stone` exhibit abrupt performance degradation beyond $BER = 10^{-4}$, while `chicken` and `wool` degrade gradually. We attribute this to task structure: sequential subtasks (e.g., tree-chopping) have deterministic action dependencies, where a single error can disrupt entire workflows. In contrast, stochastic tasks (e.g., animal interaction) inherently tolerate variability, alleviating the impact of errors. Thus, error resilience correlates with subtask-specific requirements and environmental randomness.

Resilience Dynamics for Execution Steps. Embodied agents often transition between critical and non-critical stages within a subtask. To investigate how error impacts vary with execution steps, we use the subtask `mine` logs as a case study and inject bit errors at different steps, as shown in Fig. 7. This subtask can be roughly divided into two phases: exploration (searching for trees) and execution (chopping trees). During exploration, as in Fig. 7(a), actions are less constrained, and errors primarily cause localized movement deviations without catastrophic failure. However, the execution stage (Fig. 7(b)) demands precise, sequential, aligned actions (e.g., striking specific tree blocks), where errors can disrupt dependencies, trigger incoherent actions (e.g., misaligned strikes), and eventually prevent task completion. This demonstrates that error severity is stage-specific and increases with task-criticality.

Discussion. The resilience behavior exhibits subtask-dependent diversity and stage-specific dynamics.

5 CREATE Framework

Building on insights from Sec. 3.1 and 4, we propose CREATE, a co-optimization design principle encompassing circuit-, model- and application-level techniques for efficient yet reliable embodied AI systems. First, *anomaly detection and clearance* (AD) at the circuit level mitigates the impact of large errors from timing violations. Next, *weight-rotation-enhanced planning* (WR) enhances the LLM’s resilience against remaining small but still critical errors. Finally, an *autonomy-aware voltage scaling* (VS) mechanism monitors the agent’s execution status and dynamically adjusts the voltage of the controller at runtime for additional power savings. Together,

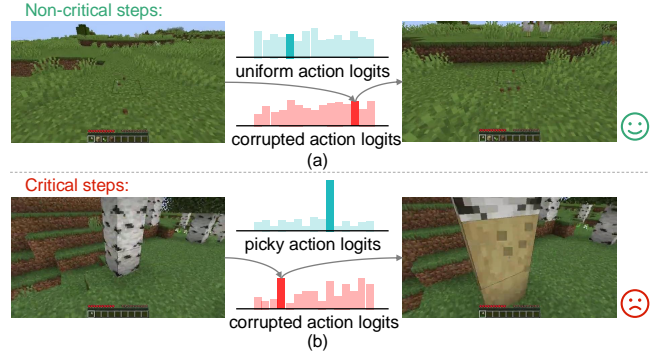


Figure 7. Stage-specific Resilience. (a) Non-critical steps exhibit uniform action logits, accommodating corruption without catastrophic failure. (b) Critical steps exhibit picky action logits, where corruptions may cause failure (e.g., failing to chop down trees).

by applying AD+WR to the planner and AD+VS to the controller, CREATE forms a tight vertical integration that delivers synergistic benefits, enabling aggressive voltage reduction without modifying operating frequency.

5.1 Anomaly Detection and Clearance

As discussed in Sec. 3.1, lowering the voltage margin often induces timing errors that predominantly flip more significant bits, causing large deviations and performance degradation. To mitigate this, we propose an *anomaly detection and clearance* (AD) mechanism that identifies out-of-bounds values and clamps them to zero.

In practice, GEMM operations in accelerators typically use lower-precision (e.g., INT8) formats and re-quantize results based on an offline-determined scaling factor [21, 22, 82]. By profiling runtime GEMM outputs throughout the entire JARVIS-1 inference pipeline (Fig. 8(a)), we observe two properties: (1) output values rarely occupy the significant bits (as in Fig. 4(b)), and (2) most elements are located near zero. Hence, if any result exceeds the known valid bound (e.g., 127 times the output scaling factor in INT8), it is flagged as an anomaly and clamped to zero. Although this does not fix faulty results, it substantially alleviates large-magnitude errors, leaving the residual discrepancy to DNNs’ inherent fault tolerance. We emphasize that the two properties mentioned above are well-documented across many DNNs during inference [57, 60, 84, 86]. Therefore, our strategy is not restricted to JARVIS-1 but can be generalizable to a wide range of embodied AI systems built upon similar DNN architectures.

We implement AD with a lightweight modification to the systolic array, which supports GEMM operation in embodied AI systems, as shown in Fig. 8(b). During GEMM computation, weights are stored in each processing element (PE), while inputs are streamed horizontally from left to right. Partial sums accumulate along columns as they propagate vertically downward, with the final results generated at the

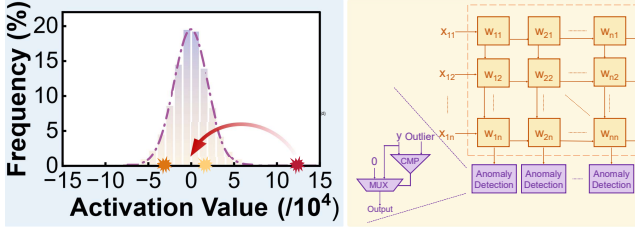


Figure 8. Anomaly Detection and Clearance. (a) Runtime GEMM results distribution. (b) Circuit design.

bottom. We augment this structure with a row of *anomaly detection units* at the output stage. Each unit consists of a comparator and a multiplexer, and the final results are checked against the valid range. Any out-of-range anomaly is clamped to zero, while in-range values pass through unchanged. This post-processing detection decouples from hardware specification and incurs minimal overhead, ensuring portable and lightweight real-time error suppression.

5.2 Weight-Rotation-Enhanced Planning

As discussed in Sec. 4.1, pre-normalization components in the planner LLM are highly vulnerable to errors. While AD in Sec. 5.1 suppresses timing errors exceeding the anomaly bound, it does not address smaller errors within the normal range that still degrade task quality. To remedy this, we propose *weight rotation-enhanced planning* (WR), a model-level approach that redistributes activation outliers via offline weight transformations.

Inspired by quantization techniques [85–88], we *rotate* activations into an outlier-free distribution via multiplication with a rotation matrix. A simple yet effective choice is the standard Hadamard matrix H [100], which is recursively defined via the Kronecker product (\otimes) [101]:

$$H_2 = \frac{1}{\sqrt{2}} \begin{bmatrix} 1 & 1 \\ 1 & -1 \end{bmatrix} \quad \text{and} \quad H_{2^k} = H_2 \otimes H_{2^{k-1}}$$

This rotation disperses outliers across dimensions, yielding more uniform activations. Crucially, since the rotation matrices can preserve the L2 norm as RMSNorm denominators, they integrate seamlessly into LLM computation without altering overall network outputs.

Our technique focuses solely on redistributing activations before normalization and avoids online rotations as in [85–88]. Fig. 9(a) depicts the required rotations, which can be merged into the weights (0 and Down) offline. For example, consider 0 with input X and weight W_0 , yielding $Y = XW_0$. By right-multiplying W_0 with H , we obtain $X(W_0H) = (XW_0)H = YH$ as an outlier-free activation in Fig. 9(b). To maintain the functional correctness of SiLU in the multi-layer perceptron (MLP) block, W_{gate} and W_{up} are left-multiplied by H^T . Similarly, to eliminate outliers after Down, W_{down} are right-multiplied by H , while W_Q, W_K and W_V in the next layer are left-multiplied by H^T . These offline procedures

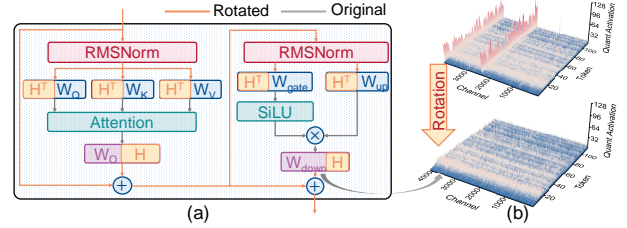


Figure 9. Weight-Rotation Enhanced Planning. (a) Weights are multiplied offline by Hadamard matrices. (b) Pre- and post-rotation activation distribution.

introduce no additional runtime overhead and require no model-specific finetuning. Additionally, rotated activations can collaborate with AD by further tightening the anomaly bound, enabling more effective error suppression.

5.3 Autonomy Adaptive Voltage Scaling

To leverage the subtask- and step-dependent resilience behavior (Sec. 4.2), we propose an *autonomous-adaptive voltage scaling* (VS) mechanism to maximize controller efficiency. We first identify the entropy [102] of action logits as a principal runtime status indicator and train a lightweight network to predict it before inference. We then introduce an LDO-based architecture for dynamic voltage adjustment with minimal circuit overhead, offering a generalizable runtime voltage scaling solution for RL-based embodied controllers.

Entropy of Action Logits as Indicator. Embodied agents typically face dynamic environments, where each step's importance varies remarkably. As in Sec. 4.2, resilience behavior differs across subtasks and dynamic execution statuses, making manually designed or fixed policies inadequate.

To design an effective voltage-control policy, a runtime metric is required to quantify step-criticality. Observing the action logits (denoted as $z \in \mathbb{R}^n$) in Fig. 7 reveals stage-dependent distributions: near-uniform logits during non-critical phases indicate low confidence, while sharply picky logits in critical phases reflect high confidence in specific actions. This motivates us to use the entropy [102], defined as $H(z) = - \sum_{i=1}^n z_i \log(z_i)$, to quantify this confidence and represent step criticality. Fig. 10 shows an example of entropy across task steps, which precisely indicates the agent's status. Lower entropy corresponds to critical stages that require robust voltage margins, whereas higher entropy indicates non-critical phases amenable to lower voltages for better efficiency. This approach dynamically aligns algorithmic certainty with system energy costs.

Entropy Predictor. To enable step-granularity voltage scaling, we introduce a pre-execution entropy predictor. Taking in the subtask prompt embedding and observed image, the entropy predictor estimates the controller's error-free entropy that avoids distortion by any prior errors. As depicted in Fig. 11(a), the predictor uses a CNN for image processing,

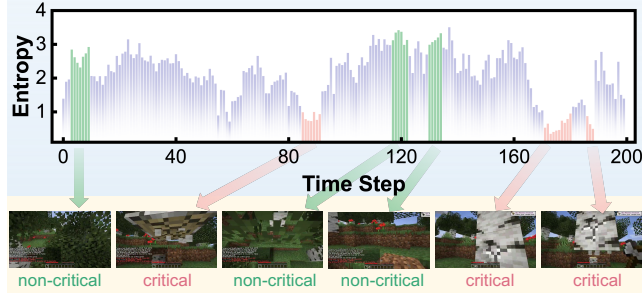


Figure 10. Entropy curve across timesteps. Higher entropy corresponds to non-critical execution steps, while lower entropy indicates critical ones.

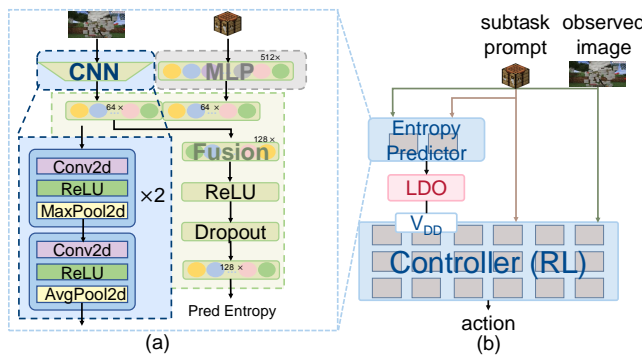


Figure 11. Autonomy-Aware Voltage Scaling. (a) Entropy predictor network architecture. (b) Voltage scaling system: an LDO dynamically adjusts the controller model’s supply voltage based on real-time entropy predictions.

an MLP for prompt embeddings, and a fusion MLP to output a single scalar entropy estimate. The model details are provided in Appendix A. We construct a dataset of over 250,000 frames from diverse tasks, each containing a prompt embedding, an observed image, and a ground-truth entropy value derived from error-free controller executions. The predictor is trained with a mean-square error (MSE) loss between the predicted and ground-truth entropy.

Voltage Scaling System. Our voltage scaling system adaptively adjusts the supply voltages of the controller model based on the predicted entropy, as shown in Fig. 11(b). The controller model and predictor all run on PE arrays, while the predictor operates at nominal voltage to ensure an error-free entropy prediction. This prediction is passed to digital LDO [93], which adjusts the controller’s operating voltage. Higher entropy triggers lower voltages, with the exact entropy-to-voltage mapping determined in Sec. 6.5. The controller’s voltage is updated every 5 steps—sufficiently frequent to track workload changes yet still sparse enough to minimize switching overhead (Sec. 6.5).

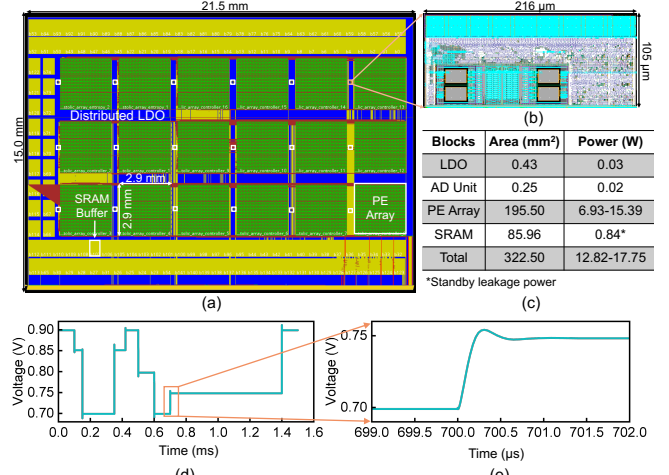


Figure 12. Hardware Platform. (a) Post-PnR layout of the full accelerator. (b) Detailed layout of LDO. (c) Area and power breakdown. (d)(e) Example voltage scaling waveforms.

6 Experiments

This section first introduces our experiment setup (Sec. 6.1), and circuit-level metrics (Sec. 6.2). We then analyze the effectiveness of the three core techniques of CREATE individually (Sec. 6.3–6.5) and their interactions via ablation studies (Sec. 6.6). We further demonstrate the overall benefits of CREATE, validating its generality across diverse tasks and embodied AI platforms (Sec. 6.7), and analyzing its real-world impact (Sec. 6.8). Finally, we discuss the sensitivity to several configurations (Sec. 6.9) and compare our proposed approach against existing methods (Sec. 6.10).

6.1 Experiment Setup

Hardware Platform. We integrate CREATE techniques in a unified hardware system designed for end-to-end embodied AI deployment, as shown in Fig. 12. Anomaly detection units in Sec. 5.1 are appended to systolic arrays with 128×128 PEs that are composed of an 8-bit multiplier and a 24-bit accumulator. The dynamic voltage scaling system required in Sec. 5.3 is supported with a distributed LDO design. Our design is synthesized with a commercial 22 nm PDK at a nominal 0.9 V supply voltage and a 2 ns clock cycle. The LDO is built based on [103] and can dynamically scale the PE array voltage from 0.6 V to 0.9 V in 10 mV steps. The LDO achieves 99.8% peak current efficiency and a 90 ns/50 mV transient response time, as listed in Table 2. On-chip SRAM buffers (142×512 KB, totaling 71 MB) are placed around the PE arrays, with HBM2 [104] used for off-chip memory. During inference, weights and inputs are initially loaded from off-chip HBM2 and cached in on-chip SRAM buffers for reuse, with activations also stored on-chip. For the controller, given the relatively small model size, our SRAM capacity can fully accommodate all weights, thereby preventing repeated off-chip memory accesses per invocation. Figs. 12(a) and (b) show

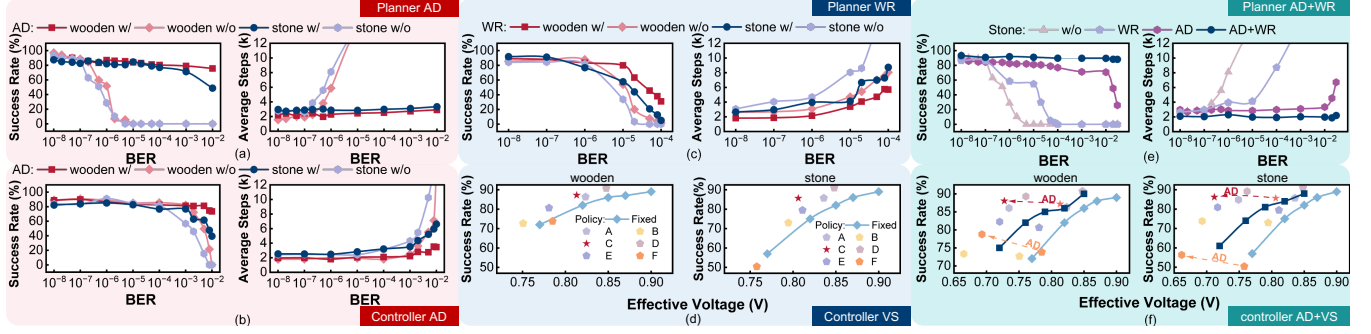


Figure 13. Evaluation of CREATE Techniques. (a) AD evaluation on the planner. (b) AD evaluation on the controller. (c) WR evaluation on the planner. (d) VS evaluation on the controller. (e) Ablation study (AD+WR) on the planner. (f) Ablation study (AD+VS) on the controller.

Table 2. Performance specifications of the LDO.

Technology	22 nm	Area	0.43 mm ²
V_{out}	0.6–0.9 V	$I_{load,max}$	15.2 A
t_{resp}	90 ns/50 mV	η_{peak}	99.8% @ $I_{load,max}$
V_{step}	10 mV	J	35 A/mm ²

t_{resp} : response time, η_{peak} : peak current efficiency, J : current density.

the Post-PnR layout of the full system and an individual LDO, respectively, with example voltage-scaling waveforms in Figs. 12(d) and (e). The area and power of primary blocks in Fig. 12(c) are reported based on post-layout simulations. Cycle-level behaviors, including inference latency and memory access, are modeled based on SCALE-Sim [105].

Entropy Predictor Training. We evaluate the proposed entropy predictor by integrating it into real-time mission episodes. In our system, the theoretical maximum entropy of action logits is 13.07, with the majority of values less than 4. For training details, we employ an MSE loss between the predicted and ground-truth entropy values, using AdamW optimizer [106] with a weight decay of 1×10^{-2} . The model is trained for 200 epochs with a batch size of 128 and an initial learning rate of 1×10^{-4} .

Evaluation Tasks. We first evaluate our framework using the fundamental wooden and stone tasks as primary benchmarks in Sec. 6.3–6.6, presenting its performance and ablation outcomes for rapid evaluation. Each experiment is repeated over 100 times to reduce randomness. To validate generality, we further test our framework on six unseen and more challenging benchmarks in JARVIS-1, which feature distinct task trajectories, providing evidence for its robustness and adaptability. To evaluate cross-platform generality, we extend our approach to separate platforms [18, 26, 27, 75] for the planner and controller. For the planner, we transplant our implementation to OpenVLA [26] on LIBERO [72] and to RoboFlamingo [27] on CALVIN [74]. For the controller, we integrate our approach with Octo [75] and RT-1 [18] on

Table 3. Performance of the full accelerator.

Peak Performance	144 TOPS	Switching Latency	540 ns
Planner MACs	5.3 T	Planner Latency	11.2 ms
Controller MACs	102 G	Controller Latency	942 μ s
Predictor MACs	43 M	Predictor Latency	8.57 μ s

TOPS: tera operations per second. MACs: multiplication-and-accumulations.

different OXE [76] tasks. Timing errors are simulated by randomly flipping bits in the accumulation results following [35, 89, 94–96]. The relation between BER and operating voltage follows Fig. 4(a).

Evaluation Metrics. We evaluate both task performance (success rate, average steps) and system efficiency (average power, total energy). Success rate measures the percentage of completed trials, while average steps denote the mean steps among all successful trials. To briefly measure the power consumption, we introduce *effective voltage*, defined as the constant voltage yielding equivalent total energy consumption to actual varying voltages. The computational energy is simulated by tracking per-step operating voltages for planner, controller, and entropy predictor execution. The switching power is negligible in practice. Failed tasks are included in energy calculations by assuming full execution.

6.2 Circuit Overhead Comparison

Fig. 12(b) presents the area and power breakdown of the proposed system. The anomaly detection units integrated into PE arrays introduce 0.08% area and 0.10% power overhead, while the LDOs distributed between arrays contribute 0.13% area and 0.14% power overhead—both negligible.

As summarized in Table 3, the full system achieves inference latencies of 11.2 ms for the planner, 942 μ s for the controller, and 8.57 μ s for the entropy predictor, respectively. Voltage switching latency remains bounded below 540 ns, which is orders of magnitude lower than the controller's inference latency. These meet our embodied AI system's 30 Hz real-time inference requirement [11].

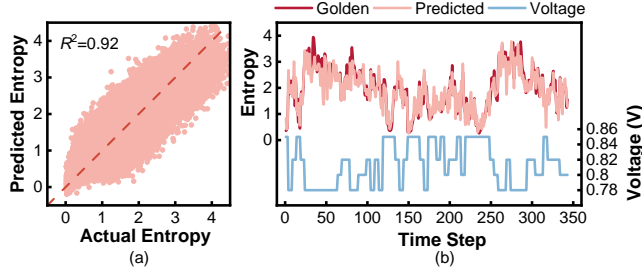


Figure 14. Entropy predictor accuracy evaluation. (a) The predicted entropy and actual entropy are strongly correlated, with $R^2 = 0.92$. (b) Real-time entropy prediction and the corresponding operating voltage level. Entropy predictor can effectively guide voltage scaling.

6.3 Anomaly Detection and Clearance Evaluation

Planner Performance Comparison. To evaluate the effectiveness of AD on the planner, Fig. 13(a) compares success rates and average steps with and without AD. AD significantly improves robustness against timing errors: at $BER = 1 \times 10^{-5}$, success rates increase from 0% to 85% for wooden and from 0% to 83% for stone, respectively, while average steps fall back to error-free scenarios. With negligible circuit overhead, AD sustains comparable performance at $BER < 1 \times 10^{-5}$, unlocking substantial potential energy savings.

Controller Performance Comparison. The impact of AD on the controller is evaluated in Fig. 13(b). AD significantly enhances the controller’s robustness: success rates improve by up to 73 and 48 percentage points for wooden and stone, while average steps are reduced by 51% and 49% at $BER = 5 \times 10^{-3}$, respectively. AD achieves particularly notable controller performance gains at $BER > 1 \times 10^{-4}$, revealing its effectiveness in mitigating timing errors under aggressive voltage scaling.

6.4 Weight Rotation Enhanced Planning Evaluation

Fig. 13(c) evaluates the impact of WR on planner reliability. By redistributing activation distributions in the LLM planner, this method prevents an individual error from drastically skewing normalization outcomes. WR improves success rates by 43% (wooden) and 40% (stone) while reducing average steps by 33% and 49% at $BER = 2 \times 10^{-5}$, respectively, which underscores the efficacy of WR in strengthening the planner’s robustness under timing errors.

6.5 Autonomy Adaptive Voltage Scaling Evaluation

Entropy Predictor Accuracy and Analysis. Our training process converges to a final $MSE = 9.96 \times 10^{-2}$. Fig. 14(a) demonstrates a strong correlation ($R^2 = 0.92$) between predicted and ground-truth entropy. Fig. 14(b) depicts the runtime performance, where the predicted entropy closely tracks actual entropy dynamics across time steps, assuring its utility for real-time voltage scaling.

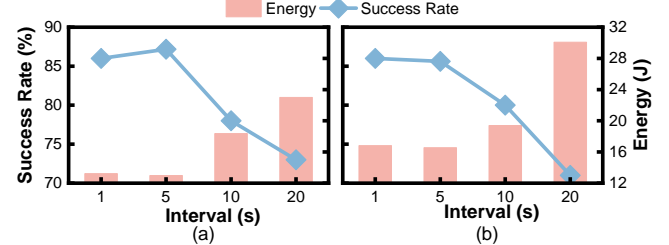


Figure 15. Voltage update interval effects on energy consumption and success rate for (a) wooden and (b) stone.

Performance Improvements. To demonstrate the impact of VS, we compare our method against a constant-voltage baseline that maintains a fixed voltage throughout execution. Task performance is measured by the success rate on the wooden and stone benchmarks, while energy efficiency is quantified by the effective voltage, as shown in Fig. 13(d). This figure includes six entropy-to-voltage mapping policies A-F (Fig. 21) identified through a search over 100 candidates, each offering a superior balance between performance and efficiency. Compared to constant-voltage policies (blue line), which exhibit declining success rates at lower voltages, our adaptive policies consistently achieve higher energy efficiency and task performance. Among them, Policy C (red star) reduces effective voltage by 7.3% without sacrificing success rates. Therefore, it is chosen as the optimal policy, which advances the reliability–efficiency Pareto frontier and serves as the default configuration in subsequent experiments.

Voltage Update Interval Analysis. This paragraph evaluates the impact of the voltage update interval, i.e., the number of steps between voltage adjustments. As shown in Fig. 15, intervals of 1 and 5 steps sustain high success rates for both tasks, whereas intervals of 10 and 20 steps degrade performance, indicating inadequate real-time response. Energy analysis further reveals that a 5-step interval incurs slightly lower overhead than a 1-step interval. Therefore, a 5-step interval strikes an optimal balance between timely adaptation and VS efficiency and is thus chosen as the default voltage update interval.

6.6 Ablation Study

We evaluate individual techniques in our framework via ablation studies. As AD and WR target the planner while AD and VS optimize the controller, we isolate their contributions by testing AD+WR and AD+VS configurations separately.

Ablation Study on Planner. As shown in Fig. 13(e), while both AD and WR can independently enhance robustness, their combination yields significantly stronger resilience, preserving task quality even at $BER = 1 \times 10^{-2}$. This not only suggests the efficacy of AD and WR separately, but also showcases a potential synergistic effect. We attribute this synergy to WR’s ability to distribute outliers across dimensions, which lowers AD’s anomaly detection threshold and further mitigates error effects.

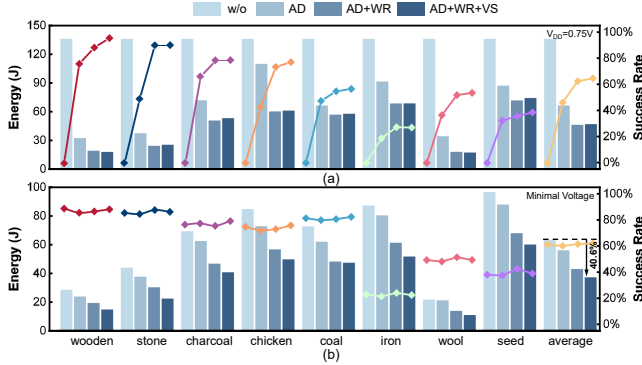


Figure 16. Overall evaluation across different tasks. (a) At 0.75 V, CREATE maintains success rates while reducing execution steps and energy consumption. (b) By supporting aggressive voltage scaling, CREATE achieves an average 40.6% energy savings without performance degradation.

Ablation Study on Controller. Fig. 13(f) compares VS combined with AD (darker lines and pentagons) against standalone VS (lighter lines and hexagons). By improving robustness at low voltages, AD enables VS to operate at further reduced voltage levels, bringing in more energy efficiency. This effect is visualized by the leftward shifts in the data points, with dashed arrows indicating reductions in effective voltage. When collaborating with AD, the optimal policy lowers effective voltage by 11.2% (wooden) and 13.2% (stone) relative to constant-voltage baselines with AD, and by 16.4% and 18.2% versus baselines without AD, all while maintaining task success rates. These results highlight another synergistic benefit of combining VS and AD.

6.7 Overall Evaluation across Different Tasks

This section evaluates the overall benefits of the entire framework. To further evaluate the generality, we extend experiments to six additional, more complex workloads within JARVIS-1, including charcoal, chicken, coal, iron, wool, and seed tasks. We first report success rates and computational energy consumption at 0.75V to demonstrate reliability improvement for low voltage operation. We then quantify efficiency gains through energy savings when operating under the lowest voltage that sustains an acceptable performance.

Reliability Improvement. Fig. 16(a) compares success rates and total computational energy consumption across four configurations and eight tasks: no protection, AD only, AD+WR, and AD+WR+VS. Operating at 0.75V without protection leads to near-zero success rates. AD alone recovers an average of 71% of the error-free success rate, while combining AD with WR boosts this reliability to 97%, closely approaching the baseline. VS, though not designed to enhance fault tolerance, adds minimal overhead. By improving task quality, total energy consumption is significantly reduced through fewer average steps.

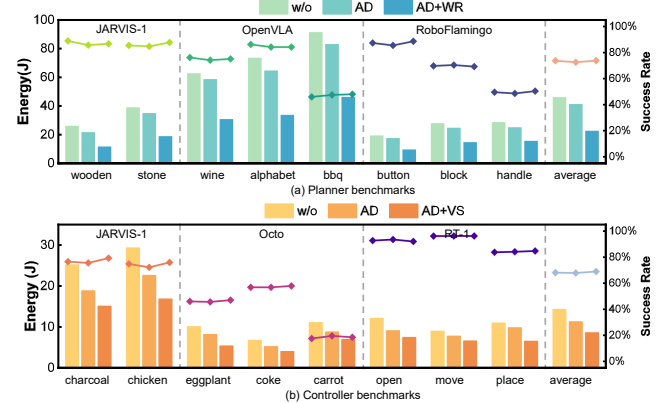


Figure 17. Cross-platform evaluation. Across various platforms and tasks, our techniques consistently achieve energy savings. AD+WR reduces planner energy consumption by 50.7% on average, while AD+VS achieves 39.3% average power savings for controllers.

Efficiency Improvement. Fig. 16(b) compares the computational energy consumption under the lowest voltages across tasks that preserves success rates. Compared to nominal voltage scenarios, AD alone results in an average 11.1% reduction in energy consumption. WR further allows much lower planner voltage, achieving 18.8% computational energy savings. VS optimizes controller voltage dynamically, contributing an additional 10.7% savings. These techniques collectively achieve 40.6% energy savings without compromising task success rates.

Cross-platform Generality Evaluation. To further validate the generality of our proposed method, we apply our techniques to additional representative embodied AI platforms. Due to limited open-source support for robust end-to-end robotic platforms that integrate both planners and controllers, we evaluate energy savings separately. For planners, we apply AD+WR to OpenVLA (wine, alphabet, bbq on LIBERO) and RoboFlamingo (button, block, handle on CALVIN). For controllers, we employ AD+VS onto Octo (eggplant, coke, carrot on OXE) and RT-1 (open, move, place on OXE). Detailed task descriptions are provided in the Appendix B. Fig. 17 shows the resulting computational energy savings while maintaining task quality. Across all platforms and tasks, our techniques consistently reduce energy consumption. AD+WR reduces planner energy consumption by 50.7% on average, while AD+VS achieves 39.3% average savings for controllers.

6.8 Energy Consumption Breakdown and Analysis
Sec. 6.7 demonstrates that our CREATE framework can consistently improve the reliability and efficiency of a wide range of embodied AI platforms. In this subsection, we analyze how these computational energy savings translate to

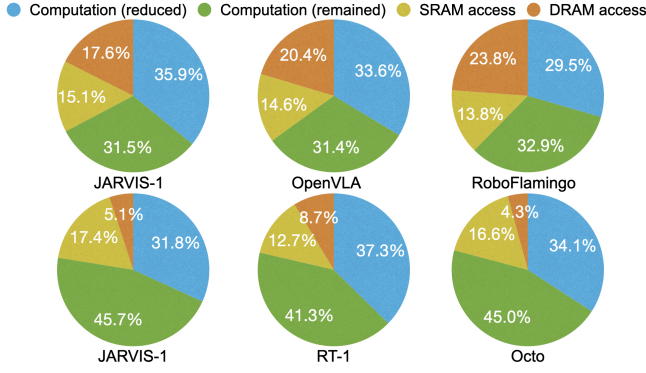


Figure 18. Chip-level energy breakdown. For planners, computation accounts for about 65% of total energy and AD+WR reduces the computation energy by about 55%, resulting in about 30% total energy savings. For controllers, computation dominates over 75% of total energy, and AD+VS achieves about 45% reduction in computation energy, translating to about 35% total energy savings.

overall chip-level energy reduction and extended battery life for the entire robotic system.

The chip-level energy consumption can be broadly divided into two components: computation and memory access, with the latter including both on-chip SRAM and off-chip DRAM accesses. Table 4 summarizes the total number of parameters and computations for all models evaluated in this work. Energy estimates are derived by combining SCALE-Sim simulation results with post-layout synthesis reports and HBM2 specifications [104]. While planner weights require off-chip loading for each inference, the controller weights can be stored entirely within on-chip SRAM, avoiding repeated off-chip accesses during execution.

Table 4. Model parameters and computational requirements

Model	#Params (M)	Input	Output	GOps ³
JARVIS-1 planner [11]	7,869	740 ¹	25 ¹	5,344
OpenVLA [26]	6,929	617 ¹	7 ¹	4,595
RoboFlamingo [27]	2,552	505 ¹	6 ¹	2,411
JARVIS-1 controller [81]	61	128 ²	-	102
RT-1 [18]	35	224 ²	-	78
Octo [75]	27	224 ²	-	76
Entropy predictor	0.055	-	-	0.043

¹The input and output sizes of the planner correspond to the representative number of prefill and decode tokens, which may vary across executions. ²For controllers, the input size refers to the resolution of square RGB images. ³Giga operations @ INT8.

Fig. 18 shows the energy breakdown for each planner and controller. Computation accounts for 67.4%, 65.0%, and 62.4% of total energy in the planners, and 77.5%, 78.6%, and 79.1% in the controllers (due to amortized DRAM overhead). Consequently, the gains profiled in Sec. 6.7 translate to chip-level

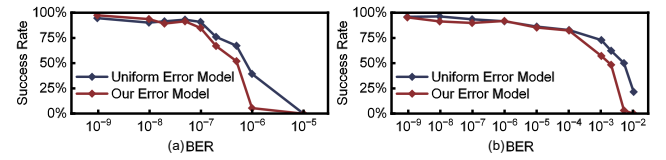


Figure 19. Comparison of uniform and hardware-specific error models applied to (a) the planner and (b) the controller on the wooden task in JARVIS-1.

energy savings of 35.9%, 33.6%, and 29.5% for the planners, and 31.8%, 37.3%, and 34.1% for the controllers, respectively.

Although some savings may be partially offset by energy consumption from mechanical components (e.g., actuators and motors), we estimate an overall battery life extension of 15–30% in realistic robotic deployments according to several popular configurations [13, 26, 30–32], where computation accounts for energy consumption comparable to or exceeding that of mechanical components. These gains come with negligible impact on task success, computational latency, or chip area, making the proposed approach a practical and meaningful optimization for real-world embodied AI deployment. Besides, this computational power reduction would also ease heat dissipation issues.

6.9 Configuration Analysis

This subsection investigates the impact of several manually defined configurations. First, we validate the conclusions drawn in Sec. 4 under uniform error model. Next, we analyze how the number of experiment repetitions affects the measured task performance. Finally, we discuss the implications of applying more aggressive quantization, such as INT4.

Validity of Resilience Characterization. In Sec. 4, we adopt a uniform error model to derive generalizable algorithmic insights, while in Sec. 6, error model profiled in Fig. 4 is used for more accurate power estimation under voltage scaling. Fig. 19 presents success rates for the wooden task, showing the impact of both error models. Although there are slight numerical differences, the overall performance trends remain consistent, validating that resilience characterization is independent of the specific error model.

Statistical significance of repetitions. In this work, we repeat our experiments for *at least* 100 times to guarantee a 95% confidence interval of 3% to 5%. This is sufficient to reveal an overall trend that supports our conclusions. Table 5 presents the measured success rate of the wooden task as the number of repeated experiments increases. As shown, 100 repetitions have been sufficient to get converged results.

Quantization-related behaviors. Although this work chooses INT8 as a default configuration, more aggressive quantization (e.g., INT4) offers an orthogonal approach to reduce power consumption and extend battery life, since it decreases not only computational complexity but also

Table 5. Measured success rates versus repetitions.

# Repetitions	20	40	60	80	90	100
Success Rate	85.0%	90.0%	91.7%	92.5%	91.1%	90.0%
# Repetitions	110	120	140	160	180	200
Success Rate	89.1%	89.2%	90.7%	90.6%	89.4%	89.5%

Measured on wooden task, $BER = 1 \times 10^{-7}$ injected to the JARVIS-1 controller.

Table 6. Success rate on stone when applying AD+WR

BER	1×10^{-6}	1×10^{-5}	1×10^{-4}	1×10^{-3}	1×10^{-2}
INT8	90.4%	91.5%	91.4%	90.5%	85.6%
INT4	91.0%	88.3%	88.2%	89.5%	87.7%

memory overhead. At the circuit level, when quantized to INT4, timing errors in higher bits would still be frequent since their critical paths are longer. At the algorithm level, we present the effects of AD+WR for INT8 and INT4 in Table 6. The current results are not statistically different. We hypothesize that this is because, compared to INT8, INT4 reduces the error-free success rate due to larger quantization error. However, after applying AD+WR, the undetected error range below the detection threshold is compressed, thereby enhancing robustness against injected errors.

6.10 Comparison with Existing Techniques

In this subsection, we compare CREATE with existing compatible circuit- and algorithm-level baselines. On the circuit level, we select a representative timing-borrowing approach, ThUnderVolt [40], and widely used DMR [39]; on the algorithm level, we adopt SOTA ABFT variants [49]. Fig. 20 shows success rates and total energy consumption across various operating voltages. DMR achieves high reliability but incurs at least 2 \times overhead and frequent error recoveries, bringing about prohibitive energy cost. ThUnderVolt adds bypass circuits to all PEs in order to skip faulty results with slightly lower circuit overhead, but because of excessive neuron pruning, it significantly degrades performance and increases execution steps that ultimately increase power consumption at low supply voltages. ABFT uses lightweight checksums to correct errors, but its application below 0.85V is confined because of frequent error recovery overhead as BER increases. In contrast, CREATE introduces negligible circuit overhead, avoids recovery mechanisms, and maintains task quality, achieving 35.0% and 33.8% energy savings for wooden and stone, respectively.

7 Conclusion

We introduce CREATE, a general design principle that exploits the heterogeneous resilience across circuit-algorithm-application layers to synergistically enable efficient yet reliable embodied AI systems. For the first time, we perform extensive error injection experiments to characterize the resilience of embodied AI systems. Our results highlight that

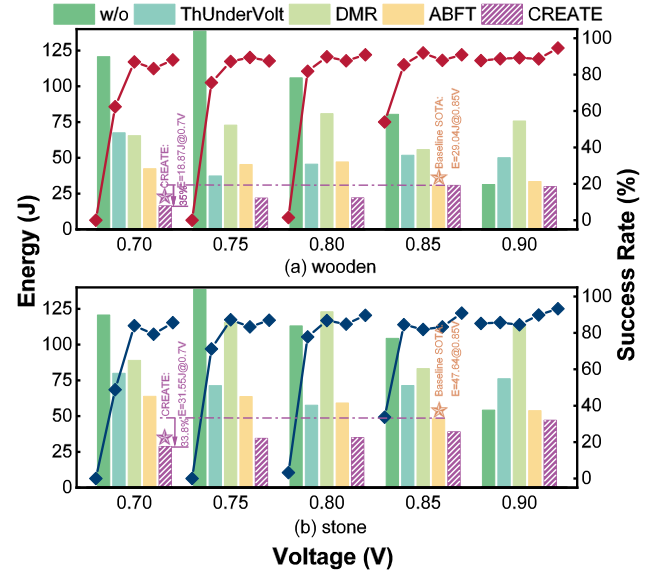


Figure 20. Existing technique comparisons. CREATE consistently outperforms all baselines across operating voltages, reducing energy consumption by (a) 35.0% for wooden and (b) 33.8% for stone over SOTA baseline.

the planner exhibits a much worse resilience than the controller due to systematic outliers in the activation distribution, while the controller's resilience exhibits a dependency on subtasks and execution steps. Building on these insights, CREATE co-optimizes efficiency and reliability across circuit, model, and application layers, with a voltage scaling architecture design. By enabling aggressive voltage reduction, CREATE consistently achieves energy savings across diverse embodied AI platforms and tasks. It reduces computational energy consumption by an average of 40.6% compared to nominal-voltage operation and 35.0% over baseline SOTA methods, which translates to 29.5% to 37.3% chip-level energy savings. By facilitating energy-efficient embodied AI deployment, our framework extends overall system battery life by about 15% to 30%, broadening the potential application scope for embodied AI systems.

Acknowledgments

This work was supported in part by the National Natural Science Foundation of China (NSFC) under Grant 62125401, Grant 62495102, Grant 92464104, and Grant 62341407; in part by the National Key Research and Development Program under Grant 2024YFB4505004; in part by the Beijing Municipal Science and Technology Program under Grant Z241100004224015; in part by the Beijing Outstanding Young Scientist Program under Grant JWZQ20240101004; and in part by the 111 Project under Grant B18001.

References

- [1] Y. Liu, W. Chen, Y. Bai, X. Liang, G. Li, W. Gao, and L. Lin, “Aligning cyber space with physical world: A comprehensive survey on embodied ai,” *arXiv preprint arXiv:2407.06886*, 2024.
- [2] J. Duan, S. Yu, H. L. Tan, H. Zhu, and C. Tan, “A survey of embodied ai: From simulators to research tasks,” *IEEE Transactions on Emerging Topics in Computational Intelligence*, vol. 6, no. 2, pp. 230–244, 2022.
- [3] Z. Xu, K. Wu, J. Wen, J. Li, N. Liu, Z. Che, and J. Tang, “A survey on robotics with foundation models: toward embodied ai,” *arXiv preprint arXiv:2402.02385*, 2024.
- [4] A. Brohan, N. Brown, J. Carbajal, Y. Chebotar, X. Chen, K. Choromanski, T. Ding, D. Driess, A. Dubey, C. Finn, *et al.*, “Rt-2: Vision-language-action models transfer web knowledge to robotic control,” *arXiv preprint arXiv:2307.15818*, 2023.
- [5] C. Gan, S. Zhou, J. Schwartz, S. Alter, A. Bhandwaldar, D. Gutfreund, D. L. Yamins, J. J. DiCarlo, J. McDermott, A. Torralba, *et al.*, “The threeworld transport challenge: A visually guided task-and-motion planning benchmark towards physically realistic embodied ai,” in *2022 International conference on robotics and automation (ICRA)*, pp. 8847–8854, IEEE, 2022.
- [6] Q. Zhou, S. Chen, Y. Wang, H. Xu, W. Du, H. Zhang, Y. Du, J. B. Tenenbaum, and C. Gan, “Hazard challenge: Embodied decision making in dynamically changing environments,” *arXiv preprint arXiv:2401.12975*, 2024.
- [7] M. Ahn, A. Brohan, N. Brown, Y. Chebotar, O. Cortes, B. David, C. Finn, C. Fu, K. Gopalakrishnan, K. Hausman, *et al.*, “Do as i can, not as i say: Grounding language in robotic affordances,” *arXiv preprint arXiv:2204.01691*, 2022.
- [8] D. Driess, F. Xia, M. S. Sajjadi, C. Lynch, A. Chowdhery, B. Ichter, A. Wahid, J. Tompson, Q. Vuong, T. Yu, *et al.*, “Palm-e: An embodied multimodal language model,” in *International Conference on Machine Learning*, pp. 8469–8488, PMLR, 2023.
- [9] C. H. Song, J. Wu, C. Washington, B. M. Sadler, W.-L. Chao, and Y. Su, “Llm-planner: Few-shot grounded planning for embodied agents with large language models,” in *Proceedings of the IEEE/CVF international conference on computer vision*, pp. 2998–3009, 2023.
- [10] G. Wang, Y. Xie, Y. Jiang, A. Mandlekar, C. Xiao, Y. Zhu, L. Fan, and A. Anandkumar, “Voyager: An open-ended embodied agent with large language models,” *arXiv preprint arXiv:2305.16291*, 2023.
- [11] Z. Wang, S. Cai, A. Liu, Y. Jin, J. Hou, B. Zhang, H. Lin, Z. He, Z. Zheng, Y. Yang, *et al.*, “Jarvis-1: Open-world multi-task agents with memory-augmented multimodal language models,” *IEEE Transactions on Pattern Analysis and Machine Intelligence*, 2024.
- [12] K. Black, N. Brown, D. Driess, A. Esmail, M. Equi, C. Finn, N. Fusai, L. Groom, K. Hausman, B. Ichter, *et al.*, “A vision-language-action flow model for general robot control,” *arXiv preprint arXiv:2410.24164*, 2024.
- [13] Y. Huang, Y. Hao, B. Yu, F. Yan, Y. Yang, F. Min, Y. Han, L. Ma, S. Liu, Q. Liu, *et al.*, “Dadu-corki: Algorithm-architecture co-design for embodied ai-powered robotic manipulation,” in *Proceedings of the 52nd Annual International Symposium on Computer Architecture*, pp. 327–343, 2025.
- [14] A. Suleiman, Z. Zhang, L. Carlone, S. Karaman, and V. Sze, “Navion: A 2-mw fully integrated real-time visual-inertial odometry accelerator for autonomous navigation of nano drones,” *IEEE Journal of Solid-State Circuits*, vol. 54, no. 4, pp. 1106–1119, 2019.
- [15] Y. Gan, Y. Bo, B. Tian, L. Xu, W. Hu, S. Liu, Q. Liu, Y. Zhang, J. Tang, and Y. Zhu, “Eudoxus: Characterizing and accelerating localization in autonomous machines industry track paper,” in *2021 IEEE International Symposium on High-Performance Computer Architecture (HPCA)*, pp. 827–840, IEEE, 2021.
- [16] J. Achiam, S. Adler, S. Agarwal, L. Ahmad, I. Akkaya, F. L. Aleman, D. Almeida, J. Altenschmidt, S. Altman, S. Anadkat, *et al.*, “Gpt-4 technical report,” *arXiv preprint arXiv:2303.08774*, 2023.
- [17] J. Wen, Y. Zhu, J. Li, M. Zhu, Z. Tang, K. Wu, Z. Xu, N. Liu, R. Cheng, C. Shen, *et al.*, “Tinyvla: Towards fast, data-efficient vision-language-action models for robotic manipulation,” *IEEE Robotics and Automation Letters*, 2025.
- [18] A. Brohan, N. Brown, J. Carbajal, Y. Chebotar, J. Dabis, C. Finn, K. Gopalakrishnan, K. Hausman, A. Herzog, J. Hsu, *et al.*, “Rt-1: Robotics transformer for real-world control at scale,” *arXiv preprint arXiv:2212.06817*, 2022.
- [19] Z. Wan, B. Yu, T. Y. Li, J. Tang, Y. Zhu, Y. Wang, A. Raychowdhury, and S. Liu, “A survey of fpga-based robotic computing,” *IEEE Circuits and Systems Magazine*, vol. 21, no. 2, pp. 48–74, 2021.
- [20] The Chinese University of Hong Kong, “Airship: Ai research and innovation hub,” <https://airs.cuhk.edu.cn/en/airship>, 2023.
- [21] N. P. Jouppi, C. Young, N. Patil, D. Patterson, G. Agrawal, R. Bajwa, S. Bates, S. Bhatia, N. Boden, A. Borchers, *et al.*, “In-datacenter performance analysis of a tensor processing unit,” in *Proceedings of the 44th annual international symposium on computer architecture*, pp. 1–12, 2017.
- [22] S. Markidis, S. W. Der Chien, E. Laure, I. B. Peng, and J. S. Vetter, “Nvidia tensor core programmability, performance & precision,” in *2018 IEEE international parallel and distributed processing symposium workshops (IPDPSW)*, pp. 522–531, IEEE, 2018.
- [23] D. McNulty, A. Hennessy, M. Li, E. Armstrong, and K. M. Ryan, “A review of li-ion batteries for autonomous mobile robots: Perspectives and outlook for the future,” *Journal of Power Sources*, vol. 545, p. 231943, 2022.
- [24] Figure AI Inc., “Helix: Advancing ai robotics.” <https://www.figure.ai/news/helix>, 2025.
- [25] Z. Wan, Y. Du, M. Ibrahim, J. Qian, J. Jabbour, Y. Zhao, T. Krishna, A. Raychowdhury, and V. J. Reddi, “Reca: Integrated acceleration for real-time and efficient cooperative embodied autonomous agents,” in *Proceedings of the 30th ACM International Conference on Architectural Support for Programming Languages and Operating Systems, Volume 2*, pp. 982–997, 2025.
- [26] M. J. Kim, K. Pertsch, S. Karamcheti, T. Xiao, A. Balakrishna, S. Nair, R. Rafailov, E. Foster, G. Lam, P. Sanketi, *et al.*, “Openvla: An open-source vision-language-action model,” *arXiv preprint arXiv:2406.09246*, 2024.
- [27] X. Li, M. Liu, H. Zhang, C. Yu, J. Xu, H. Wu, C. Cheang, Y. Jing, W. Zhang, H. Liu, *et al.*, “Vision-language foundation models as effective robot imitators,” *arXiv preprint arXiv:2311.01378*, 2023.
- [28] J. Ting, M. Kim, J. Zhu, H. Sheng, and Z. Zhang, “Hiper: Hierarchically-composed processing for efficient robot learning-based control,” in *Proceedings of the 52nd Annual International Symposium on Computer Architecture*, pp. 313–326, 2025.
- [29] Y. Yue, Y. Wang, B. Kang, Y. Han, S. Wang, S. Song, J. Feng, and G. Huang, “Deer-vla: Dynamic inference of multimodal large language models for efficient robot execution,” *Advances in Neural Information Processing Systems*, vol. 37, pp. 56619–56643, 2024.
- [30] J. Jabbour and V. Janapa Reddi, “Generative ai agents in autonomous machines: A safety perspective,” in *Proceedings of the 43rd IEEE/ACM International Conference on Computer-Aided Design*, pp. 1–13, 2024.
- [31] ANYbotics, *ANYmal Technical Specifications*. ANYbotics, 12 2023. Accessed: 2024-09-19.
- [32] C. Gaz, M. Cognetti, A. Oliva, P. R. Giordano, and A. De Luca, “Dynamic identification of the franka emika panda robot with retrieval of feasible parameters using penalty-based optimization,” *IEEE Robotics and Automation Letters*, vol. 4, no. 4, pp. 4147–4154, 2019.
- [33] H. D. Dixit, S. Pendharkar, M. Beardon, C. Mason, T. Chakravarthy, B. Muthiah, and S. Sankar, “Silent data corruptions at scale,” *arXiv preprint arXiv:2102.11245*, 2021.
- [34] I. Moghaddasi, S. Gorgin, and J.-A. Lee, “Dependable dnn accelerator for safety-critical systems: A review on the aging perspective,” *IEEE Access*, 2023.

[35] X. Jiao, A. Rahimi, Y. Jiang, J. Wang, H. Fatemi, J. P. De Gyvez, and R. K. Gupta, “Clim: A cross-level workload-aware timing error prediction model for functional units,” *IEEE Transactions on Computers*, vol. 67, no. 6, pp. 771–783, 2017.

[36] R. Huang, X. Jiang, S. Guo, P. Ren, P. Hao, Z. Yu, Z. Zhang, Y. Wang, and R. Wang, “Variability-and-reliability-aware design for 16/14nm and beyond technology,” in *2017 IEEE International Electron Devices Meeting (IEDM)*, pp. 12–4, IEEE, 2017.

[37] F. Libano, B. Wilson, J. Anderson, M. J. Wirthlin, C. Cazzaniga, C. Frost, and P. Rech, “Selective hardening for neural networks in fpgas,” *IEEE Transactions on Nuclear Science*, vol. 66, no. 1, pp. 216–222, 2018.

[38] N. Khoshavi, A. Roohi, C. Broyles, S. Sargolzaei, Y. Bi, and D. Z. Pan, “Shieldenn: Online accelerated framework for fault-tolerant deep neural network architectures,” in *2020 57th ACM/IEEE Design Automation Conference (DAC)*, pp. 1–6, IEEE, 2020.

[39] E. Talpes, D. D. Sarma, G. Venkataramanan, P. Bannon, B. McGee, B. Floering, A. Jalote, C. Hsiong, S. Arora, A. Gorti, et al., “Compute solution for tesla’s full self-driving computer,” *IEEE Micro*, vol. 40, no. 2, pp. 25–35, 2020.

[40] J. Zhang, K. Rangineni, Z. Ghodsi, and S. Garg, “Thundervolt: enabling aggressive voltage underscaling and timing error resilience for energy efficient deep learning accelerators,” in *Proceedings of the 55th Annual Design Automation Conference*, pp. 1–6, 2018.

[41] J. J. Zhang, K. Basu, and S. Garg, “Fault-tolerant systolic array based accelerators for deep neural network execution,” *IEEE Design & Test*, vol. 36, no. 5, pp. 44–53, 2019.

[42] P. Pandey, P. Basu, K. Chakraborty, and S. Roy, “Greentpu: Improving timing error resilience of a near-threshold tensor processing unit,” in *Proceedings of the 56th Annual Design Automation Conference 2019*, pp. 1–6, 2019.

[43] D. Ernst, N. S. Kim, S. Das, S. Pant, R. Rao, T. Pham, C. Ziesler, D. Blaauw, T. Austin, K. Flautner, et al., “Razor: A low-power pipeline based on circuit-level timing speculation,” in *Proceedings. 36th Annual IEEE/ACM International Symposium on Microarchitecture, 2003. MICRO-36*, pp. 7–18, IEEE, 2003.

[44] N. D. Gundu, T. Shabanian, P. Basu, P. Pandey, S. Roy, K. Chakraborty, and Z. Zhang, “Effort: Enhancing energy efficiency and error resilience of a near-threshold tensor processing unit,” in *2020 25th Asia and South Pacific Design Automation Conference (ASP-DAC)*, pp. 241–246, IEEE, 2020.

[45] P. N. Whatmough, S. K. Lee, D. Brooks, and G.-Y. Wei, “Dnn engine: A 28-nm timing-error tolerant sparse deep neural network processor for iot applications,” *IEEE Journal of Solid-State Circuits*, vol. 53, no. 9, pp. 2722–2731, 2018.

[46] K.-H. Huang and J. A. Abraham, “Algorithm-based fault tolerance for matrix operations,” *IEEE transactions on computers*, vol. 100, no. 6, pp. 518–528, 1984.

[47] S. Bal, C. S. Mummidi, V. D. C. Ferreira, S. Srinivasan, and S. Kundu, “A novel fault-tolerant architecture for tiled matrix multiplication,” in *2023 Design, Automation & Test in Europe Conference & Exhibition (DATE)*, pp. 1–6, IEEE, 2023.

[48] M. Safarpour, R. Inanlou, and O. Silvén, “Algorithm level error detection in low voltage systolic array,” *IEEE Transactions on Circuits and Systems II: Express Briefs*, vol. 69, no. 2, pp. 569–573, 2021.

[49] X. Xue, C. Liu, H. Huang, B. Liu, Y. Wang, B. Yang, T. Luo, L. Zhang, H. Li, and X. Li, “Approxabft: Approximate algorithm-based fault tolerance for vision transformers,” *arXiv preprint arXiv:2302.10469*, 2023.

[50] C. Schorn, A. Guntoro, and G. Ascheid, “An efficient bit-flip resilience optimization method for deep neural networks,” in *2019 Design, Automation & Test in Europe Conference & Exhibition (DATE)*, pp. 1507–1512, IEEE, 2019.

[51] S. Kim, P. Howe, T. Moreau, A. Alaghi, L. Ceze, and V. Sathe, “Matic: Learning around errors for efficient low-voltage neural network accelerators,” in *2018 Design, Automation & Test in Europe Conference & Exhibition (DATE)*, pp. 1–6, IEEE, 2018.

[52] Z. He, J. Lin, R. Ewetz, J.-S. Yuan, and D. Fan, “Noise injection adaption: End-to-end reram crossbar non-ideal effect adaption for neural network mapping,” in *Proceedings of the 56th Annual Design Automation Conference 2019*, pp. 1–6, 2019.

[53] Z. Wan, N. Chandramoorthy, K. Swaminathan, P.-Y. Chen, K. Bhardwaj, V. J. Reddi, and A. Raychowdhury, “Mulberry: Enabling bit-error robustness for energy-efficient multi-agent autonomous systems,” in *Proceedings of the 29th ACM International Conference on Architectural Support for Programming Languages and Operating Systems, Volume 2*, pp. 746–762, 2024.

[54] S. Jha, S. Cui, T. Tsai, S. K. S. Hari, M. B. Sullivan, Z. T. Kalbarczyk, S. W. Keckler, and R. K. Iyer, “Exploiting temporal data diversity for detecting safety-critical faults in av compute systems,” in *2022 52nd Annual IEEE/IFIP International Conference on Dependable Systems and Networks (DSN)*, pp. 88–100, IEEE, 2022.

[55] Z. Wan, Y. Gan, B. Yu, S. Liu, A. Raychowdhury, and Y. Zhu, “The vulnerability-adaptive protection paradigm,” *Communications of the ACM*, vol. 67, no. 9, pp. 66–77, 2024.

[56] D. Shah, Z. Y. Xue, K. Pattabiraman, and T. M. Aamodt, “Characterizing and improving resilience of accelerators to memory errors in autonomous robots,” *ACM Transactions on Cyber-Physical Systems*, vol. 8, no. 3, pp. 1–33, 2024.

[57] G. Li, S. K. S. Hari, M. Sullivan, T. Tsai, K. Pattabiraman, J. Emer, and S. W. Keckler, “Understanding error propagation in deep learning neural network (dnn) accelerators and applications,” in *Proceedings of the International Conference for High Performance Computing, Networking, Storage and Analysis*, pp. 1–12, 2017.

[58] B. Reagen, U. Gupta, L. Pentecost, P. Whatmough, S. K. Lee, N. Mulholland, D. Brooks, and G.-Y. Wei, “Ares: A framework for quantifying the resilience of deep neural networks,” in *Proceedings of the 55th Annual Design Automation Conference*, pp. 1–6, 2018.

[59] A. Mahmoud, S. K. S. Hari, C. W. Fletcher, S. V. Adve, C. Sakr, N. R. Shanbhag, P. Molchanov, M. B. Sullivan, T. Tsai, and S. W. Keckler, “Optimizing selective protection for cnn resilience,” in *ISSRE*, pp. 127–138, 2021.

[60] Z. Wan, A. Anwar, Y.-S. Hsiao, T. Jia, V. J. Reddi, and A. Raychowdhury, “Analyzing and improving fault tolerance of learning-based navigation systems,” in *2021 58th ACM/IEEE Design Automation Conference (DAC)*, pp. 841–846, IEEE, 2021.

[61] U. K. Agarwal, A. Chan, and K. Pattabiraman, “Resilience assessment of large language models under transient hardware faults,” in *2023 IEEE 34th International Symposium on Software Reliability Engineering (ISSRE)*, pp. 659–670, IEEE, 2023.

[62] T. Xie, J. Zhao, Z. Wan, Z. Zhang, Y. Wang, R. Wang, R. Huang, and M. Li, “Realm: Reliable and efficient large language model inference with statistical algorithm-based fault tolerance,” in *2025 62nd ACM/IEEE Design Automation Conference (DAC)*, pp. 1–7, 2025.

[63] A. Chowdhery, S. Narang, J. Devlin, M. Bosma, G. Mishra, A. Roberts, P. Barham, H. W. Chung, C. Sutton, S. Gehrmann, et al., “Palm: Scaling language modeling with pathways,” *Journal of Machine Learning Research*, vol. 24, no. 240, pp. 1–113, 2023.

[64] D. Kalashnikov, J. Varley, Y. Chebotar, B. Swanson, R. Jonschkowski, C. Finn, S. Levine, and K. Hausman, “Mt-opt: Continuous multi-task robotic reinforcement learning at scale,” *arXiv preprint arXiv:2104.08212*, 2021.

[65] M. Shridhar, J. Thomason, D. Gordon, Y. Bisk, W. Han, R. Mottaghi, L. Zettlemoyer, and D. Fox, “Alfred: A benchmark for interpreting grounded instructions for everyday tasks,” in *Proceedings of the IEEE/CVF conference on computer vision and pattern recognition*, pp. 10740–10749, 2020.

[66] C. Lynch, A. Wahid, J. Tompson, T. Ding, J. Betker, R. Baruch, T. Armstrong, and P. Florence, “Interactive language: Talking to robots in real time,” *IEEE Robotics and Automation Letters*, 2023.

[67] T. Brown, B. Mann, N. Ryder, M. Subbiah, J. D. Kaplan, P. Dhariwal, A. Neelakantan, P. Shyam, G. Sastry, A. Askell, *et al.*, “Language models are few-shot learners,” *Advances in neural information processing systems*, vol. 33, pp. 1877–1901, 2020.

[68] V. Blukis, C. Paxton, D. Fox, A. Garg, and Y. Artzi, “A persistent spatial semantic representation for high-level natural language instruction execution,” in *Conference on Robot Learning*, pp. 706–717, PMLR, 2022.

[69] X. Chen, J. Djolonga, P. Padlewski, B. Mustafa, S. Changpinyo, J. Wu, C. R. Ruiz, S. Goodman, X. Wang, Y. Tay, *et al.*, “Pali-x: On scaling up a multilingual vision and language model,” *arXiv preprint arXiv:2305.18565*, 2023.

[70] W. H. Guss, B. Houghton, N. Topin, P. Wang, C. Codel, M. Veloso, and R. Salakhutdinov, “Minerl: a large-scale dataset of minecraft demonstrations,” in *Proceedings of the 28th International Joint Conference on Artificial Intelligence*, pp. 2442–2448, 2019.

[71] H. Liu, C. Li, Q. Wu, and Y. J. Lee, “Visual instruction tuning,” *Advances in neural information processing systems*, vol. 36, pp. 34892–34916, 2023.

[72] B. Liu, Y. Zhu, C. Gao, Y. Feng, Q. Liu, Y. Zhu, and P. Stone, “Libero: Benchmarking knowledge transfer for lifelong robot learning,” *Advances in Neural Information Processing Systems*, vol. 36, pp. 44776–44791, 2023.

[73] A. Awadalla, I. Gao, J. Gardner, J. Hessel, Y. Hanafy, W. Zhu, K. Marathe, Y. Bitton, S. Gadre, S. Sagawa, *et al.*, “Openflamingo: An open-source framework for training large autoregressive vision-language models,” *arXiv preprint arXiv:2308.01390*, 2023.

[74] O. Mees, L. Hermann, E. Rosete-Beas, and W. Burgard, “Calvin: A benchmark for language-conditioned policy learning for long-horizon robot manipulation tasks,” *IEEE Robotics and Automation Letters*, vol. 7, no. 3, pp. 7327–7334, 2022.

[75] D. Ghosh, H. R. Walke, K. Pertsch, K. Black, O. Mees, S. Dasari, J. Hejna, T. Kreiman, C. Xu, J. Luo, *et al.*, “Octo: An open-source generalist robot policy,” in *Robotics: Science and Systems*, 2024.

[76] A. O’Neill, A. Rehman, A. Maddukuri, A. Gupta, A. Padalkar, A. Lee, A. Pooley, A. Gupta, A. Mandlekar, A. Jain, *et al.*, “Open x-embodiment: Robotic learning datasets and rt-x models: Open x-embodiment collaboration 0,” in *2024 IEEE International Conference on Robotics and Automation (ICRA)*, pp. 6892–6903, IEEE, 2024.

[77] J. Huang, S. Yong, X. Ma, X. Linghu, P. Li, Y. Wang, Q. Li, S.-C. Zhu, B. Jia, and S. Huang, “An embodied generalist agent in 3d world,” in *Proceedings of the 41st International Conference on Machine Learning*, pp. 20413–20451, 2024.

[78] W.-L. Chiang, Z. Li, Z. Lin, Y. Sheng, Z. Wu, H. Zhang, L. Zheng, S. Zhuang, Y. Zhuang, J. E. Gonzalez, *et al.*, “Vicuna: An open-source chatbot impressing gpt-4 with 90% “chatgpt quality,” See <https://vicuna.lmsys.org> (accessed 14 April 2023), vol. 2, no. 3, p. 6, 2023.

[79] D. Z. Chen, A. X. Chang, and M. Nießner, “Scanrefer: 3d object localization in rgb-d scans using natural language,” in *European conference on computer vision*, pp. 202–221, Springer, 2020.

[80] S. K. Ramakrishnan, A. Gokaslan, E. Wijmans, O. Maksymets, A. Clegg, J. M. Turner, E. Undersander, W. Galuba, A. Westbury, A. X. Chang, M. Savva, Y. Zhao, and D. Batra, “Habitat-matterport 3d dataset (HM3d): 1000 large-scale 3d environments for embodied AI,” in *Thirty-fifth Conference on Neural Information Processing Systems Datasets and Benchmarks Track*, 2021.

[81] S. Lifshitz, K. Paster, H. Chan, J. Ba, and S. McIlraith, “Steve-1: A generative model for text-to-behavior in minecraft,” *Advances in Neural Information Processing Systems*, vol. 36, pp. 69900–69929, 2023.

[82] G. Xiao, J. Lin, M. Seznec, H. Wu, J. Demouth, and S. Han, “Smoothquant: Accurate and efficient post-training quantization for large language models,” in *International Conference on Machine Learning*, pp. 38087–38099, PMLR, 2023.

[83] J. Lin, J. Tang, H. Tang, S. Yang, X. Dang, and S. Han, “Awq: Activation-aware weight quantization for llm compression and acceleration,” *arXiv preprint arXiv:2306.00978*, 2023.

[84] Z. Yuan, L. Niu, J. Liu, W. Liu, X. Wang, Y. Shang, G. Sun, Q. Wu, J. Wu, and B. Wu, “Rptq: Reorder-based post-training quantization for large language models,” *arXiv preprint arXiv:2304.01089*, 2023.

[85] Z. Liu, C. Zhao, I. Fedorov, B. Soran, D. Choudhary, R. Krishnamoorthi, V. Chandra, Y. Tian, and T. Blankevoort, “Spinquant: Llm quantization with learned rotations,” *arXiv preprint arXiv:2405.16406*, 2024.

[86] S. Ashkboos, A. Mohtashami, M. Croci, B. Li, P. Cameron, M. Jaggi, D. Alistarh, T. Hoefler, and J. Hensman, “Quarot: Outlier-free 4-bit inference in rotated llms,” *Advances in Neural Information Processing Systems*, vol. 37, pp. 100213–100240, 2024.

[87] A. Tseng, J. Chee, Q. Sun, V. Kuleshov, and C. De Sa, “Quip #: Even better llm quantization with hadamard incoherence and lattice codebooks,” in *International Conference on Machine Learning*, pp. 48630–48656, PMLR, 2024.

[88] S. Kim, Y. Choi, J. Oh, B. Kim, and H.-J. Yoo, “Lightrot: A light-weighted rotation scheme and architecture for accurate low-bit large language model inference,” *IEEE Journal on Emerging and Selected Topics in Circuits and Systems*, 2025.

[89] Z. Zhang, R. Wei, M. Li, Y. Lin, R. Wang, and R. Huang, “Read: Reliability-enhanced accelerator dataflow optimization using critical input pattern reduction,” in *2023 IEEE/ACM International Conference on Computer Aided Design (ICCAD)*, pp. 1–9, IEEE, 2023.

[90] J.-S. Kim and J.-S. Yang, “Dris-3: Deep neural network reliability improvement scheme in 3d die-stacked memory based on fault analysis,” in *Proceedings of the 56th Annual Design Automation Conference 2019*, pp. 1–6, 2019.

[91] S.-T. Zhou, S. Katariya, H. Ghasemi, S. Draper, and N. S. Kim, “Minimizing total area of low-voltage sram arrays through joint optimization of cell size, redundancy, and ecc,” in *2010 IEEE International Conference on Computer Design*, pp. 112–117, IEEE, 2010.

[92] M. C. Casey, B. L. Bhuva, S. A. Nation, O. A. Amusan, T. D. Loveless, L. W. Massengill, D. McMorrow, and J. S. Melinger, “Single-event effects on ultra-low power cmos circuits,” in *2009 IEEE International Reliability Physics Symposium*, pp. 194–198, IEEE, 2009.

[93] T. Tambe, C. Hooper, L. Pentecost, T. Jia, E.-Y. Yang, M. Donato, V. Sanh, P. Whatmough, A. M. Rush, D. Brooks, *et al.*, “Edgebert: Sentence-level energy optimizations for latency-aware multi-task nlp inference,” in *MICRO-54: 54th Annual IEEE/ACM International Symposium on Microarchitecture*, pp. 830–844, 2021.

[94] B. Sangchoulie, K. Pattabiraman, and J. Karlsson, “One bit is (not) enough: An empirical study of the impact of single and multiple bit-flip errors,” in *2017 47th Annual IEEE/IFIP International Conference on Dependable Systems and Networks (DSN)*, pp. 97–108, IEEE, 2017.

[95] Y. He, P. Balaprakash, and Y. Li, “Fidelity: Efficient resilience analysis framework for deep learning accelerators,” in *2020 53rd Annual IEEE/ACM International Symposium on Microarchitecture (MICRO)*, pp. 270–281, IEEE, 2020.

[96] Y. S. Hsiao, Z. Wan, T. Jia, R. Ghosal, A. Mahmoud, A. Raychowdhury, V. J. Reddi, *et al.*, “Silent data corruption in robot operating system: A case for end-to-end system-level fault analysis using autonomous uavs,” *IEEE Transactions on Computer-Aided Design of Integrated Circuits and Systems*, 2023.

[97] G. Papadimitriou and D. Gizopoulos, “Demystifying the system vulnerability stack: Transient fault effects across the layers,” in *2021 ACM/IEEE 48th Annual International Symposium on Computer Architecture (ISCA)*, pp. 902–915, IEEE, 2021.

[98] R. W. Hamming, “Error detecting and error correcting codes,” *The Bell system technical journal*, vol. 29, no. 2, pp. 147–160, 1950.

[99] P. H. Hochschild, P. Turner, J. C. Mogul, R. Govindaraju, P. Ranaganathan, D. E. Culler, and A. Vahdat, “Cores that don’t count,” in *Proceedings of the Workshop on Hot Topics in Operating Systems*, pp. 9–16, 2021.

[100] A. Hedayat and W. D. Wallis, “Hadamard matrices and their applications,” *The annals of statistics*, pp. 1184–1238, 1978.

[101] C. F. Van Loan, “The ubiquitous kronecker product,” *Journal of computational and applied mathematics*, vol. 123, no. 1-2, pp. 85–100, 2000.

[102] R. B. Ash, *Information theory*. Courier Corporation, 2012.

[103] S. J. Kim, D. Kim, Y. Pu, C. Shi, S. B. Chang, and M. Seok, “0.5–1-v, 90–400-ma, modular, distributed, 3×3 digital ldos based on event-driven control and domino sampling and regulation,” *IEEE Journal of Solid-State Circuits*, vol. 56, no. 9, pp. 2781–2794, 2021.

[104] H. Jun, J. Cho, K. Lee, H.-Y. Son, K. Kim, H. Jin, and K. Kim, “Hbm (high bandwidth memory) dram technology and architecture,” in *2017 IEEE International Memory Workshop (IMW)*, pp. 1–4, IEEE, 2017.

[105] A. Samajdar, Y. Zhu, P. Whatmough, M. Mattina, and T. Krishna, “Scale-sim: Systolic cnn accelerator simulator,” *arXiv preprint arXiv:1811.02883*, 2018.

[106] I. Loshchilov and F. Hutter, “Decoupled weight decay regularization,” 2019.

A Model Details

This work involves multiple models, whose detailed architecture, such as the number of layers, hidden dimensions, parameters, and FLOPs, are critical hyperparameters. Table 7 to 9 presents the detailed architectures of the planner, controller, and our proposed entropy predictor. Table 4 further summarizes the total number of parameters and computations for each model. For brevity, only primary modules are listed, with some secondary components omitted. The kernel size of Conv2d is 3 by default.

Table 7. Model architecture of planners

Model	#Layers	Hidden Dim	MLP Dim
JARVIS-1	32	4,096	14,336
OpenVLA	32	4,096	11,008
RoboFlamingo	24	2,048	8,192

Table 8. Model architecture of controllers

Model	Parts	# Layers	Hidden Dim	MLP Dim
JARVIS-1	Img*	10	3-256	128-256
	Decoder	4	1,024	4,096
RT-1	MaxViT	11	64-768	384-3,072
	FiLM	23	1,536	256-3,072
	ViT	6	768	3,072
Octo	T5	12	384	1,152
	Obs*	8	6-384	32-512
	Head	3	256	1,024

*Conv2d layers, where the hidden and MLP dim refer to input and output channels.

B Task Description

This paper evaluates 21 tasks across four benchmarks, which are referred to as abbreviations throughout this paper for brevity. Detailed task descriptions are provided in Table 10.

Table 9. Model architecture of the entropy predictor

Block	Layer Type	Configuration
Image Processing (CNN)	Conv2d	in=3, out=16, stride=3, padding=1
	ReLU	
	MaxPool2d	kernel_size=2
	Conv2d	in=16, out=32, stride=3, padding=1
	ReLU	kernel_size=2
	MaxPool2d	in=32, out=64, stride=3, padding=1
Prompt MLP	Conv2d	output_size=1
	ReLU	
Fusion MLP	AvgPool2d	
	Linear	in=512, out=64
	Concat	
	Linear	in=128, out=128
	ReLU	
	Linear	in=128, out=1

Table 10. Task descriptions

Benchmark	Abbr.	Task Description
Minecraft	wooden	Obtain a wooden pickaxe in a jungle
	stone	Obtain a stone pickaxe in the plains
	charcoal	Obtain charcoal in the plains
	chicken	Obtain a cooked chicken in the plains
	coal	Obtain coal in a savanna
	iron	Obtain an iron sword in the plains
	wool	Obtain 5 white wool in the plains
	seed	Obtain 10 wheat seeds in a savanna
	log	Obtain 10 logs in a forest
LIBERO	wine	Put wine bottle on top of cabinet
	alphabet	Pick up alphabet soup and place it in basket
CALVIN	bbq	Pick up bbq sauce and place it in basket
	button	Press the button to turn off the LED light
	block	Slide the block that it falls into the drawer
	handle	Pull the handle to open the drawer
OXE	eggplant	Put eggplant in basket
	coke	Grasp single opened coke can
	carrot	Put carrot on plate
	open	Open middle drawer
	move	Move near google baked tex
	place	Place into closed top drawer

C Entropy-to-Voltage Mapping Policy

Fig. 21 illustrates the detailed entropy-to-voltage mapping policies A to F for JARVIS-1, which are searched from over 100 candidates.

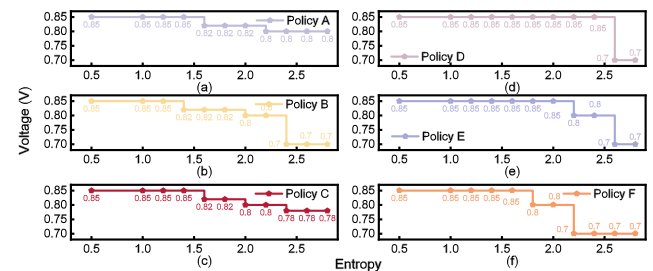


Figure 21. Selected entropy to voltage mapping policies